

www.advmat.de

ADVANCED MATERIALS



iSens: A Fiber-Based, Highly Permeable and Imperceptible Sensor Design

Thomas Stockinger, Daniela Wirthl, Guoyong Mao, Michael Drack, Roland Pruckner, Stepan Demchyshyn, Melanie Steiner, Florian Egger, Uwe Müller, Reinhard Schwödiauer, Siegfried Bauer, Nikita Arnold, and Martin Kaltenbrunner*

Embedded sensors are key to optimizing processes and products; they collect data that allow time, energy, and materials to be saved, thereby reducing costs. After production, they remain in place and are used to monitor the long-term structural health of buildings or aircraft. Fueled by climate change, sustainable construction materials such as wood and fiber composites are gaining importance. Current sensors are not optimized for use with these materials and often act as defects that cause catastrophic failures. Here, flexible, highly permeable, and imperceptible sensors (iSens) are introduced that integrate seamlessly into a component. Their porous substrates are readily infused with adhesives and withstand harsh conditions. In situ resistive temperature measurements and capacitive sensing allows monitoring of adhesives curing as used in wooden structures and fiber composites. The devices also act as heating elements to reduce the hardening time of the glue. Results are analyzed using numerical simulations and theoretical analysis. The suggested iSens technology is widely applicable and represents a step towards realizing the Internet of Things for construction materials.

1. Introduction

Sensors have become integral to our daily lives and are in continuous and ubiquitous use: They automatically switch on the lights when a person enters a house,^[1] operate in moving vehicles to recognize pedestrians at the roadside^[2] and help to control smartphones.^[3] In industry, sensors are implemented to control and optimize production processes. This reduces both costs and the emissions of greenhouse gases and improves the ecological footprint of the products. The same benefits are achieved by using wooden elements in building construction^[4] and fiber-reinforced composites in the automotive industry to make cars lighter and more efficient.^[5] Adhesive bonds play a major role both in the production of wooden structures and in fiber compos-

ites. The performance of a bond is highly dependent on the key parameters of the curing process of the adhesive such as, for example, temperature, pressure, and time. In order to characterize this process, sensors are inserted directly into the adhesive bonds.^[6,7] Ideally, the sensor is not only a powerful tool for optimizing the production process by tracking the curing data, but remains in the component for its entire lifetime, providing data for structural health monitoring (SHM)^[8,9] related to various parameters of surrounding materials in its vicinity (humidity, temperature, cracks), and for building information modeling (BIM).^[10] In warranty cases, the data obtained from production can also be used to confirm correct manufacturing of the parts. As a permanent part of the component, the sensor should be integrated seamlessly and influence the component as little as possible and not act as a structural defect.^[11] Previous work in this field has demonstrated sensors printed on paper which are able to measure humidity, however, the substrates used have very limited permeability.^[12,13] Poly(vinyl alcohol)-based nanomesh conductors employed as on-skin sensors are permeable to water vapor,^[14,15] but may have insufficient mechanical strength to withstand harsh operating conditions.

Here, we present imperceptible sensors (iSens) on porous substrates, more specifically, on ultra-thin paper (**Figure 1a**) and glass fiber sheets (**Figure 1b**). The sensors are designed to perform dielectric analysis for continuous in-process monitoring of the curing of an adhesive and to measure its temperature.

T. Stockinger, Dr. D. Wirthl, Dr. G. Mao, Dr. M. Drack, R. Pruckner, S. Demchyshyn, F. Egger, Dr. R. Schwödiauer, Prof. S. Bauer,^[†] Dr. N. Arnold, Prof. M. Kaltenbrunner
Soft Matter Physics


Institute of Experimental Physics
Johannes Kepler University Linz
Altenberger Straße 69, Linz 4040, Austria
E-mail: martin.kaltenbrunner@jku.at

T. Stockinger, Dr. D. Wirthl, Dr. G. Mao, Dr. M. Drack, R. Pruckner, S. Demchyshyn, F. Egger, Dr. R. Schwödiauer, Dr. N. Arnold, Prof. M. Kaltenbrunner

Soft Materials Lab
Linz Institute of Technology LIT
Johannes Kepler University Linz
Altenberger Straße 69, Linz 4040, Austria

T. Stockinger, Dr. D. Wirthl
sendance GmbH
Altenberger Straße 69, Linz 4040, Austria

M. Steiner, Dr. U. Müller
Kompetenzzentrum Holz GmbH
Altenbergerstraße 69, Linz 4040, Austria

 The ORCID identification number(s) for the author(s) of this article can be found under <https://doi.org/10.1002/adma.202102736>.

© 2021 The Authors. Advanced Materials published by Wiley-VCH GmbH. This is an open access article under the terms of the Creative Commons Attribution-NonCommercial License, which permits use, distribution and reproduction in any medium, provided the original work is properly cited and is not used for commercial purposes.

^[†]deceased

DOI: 10.1002/adma.202102736

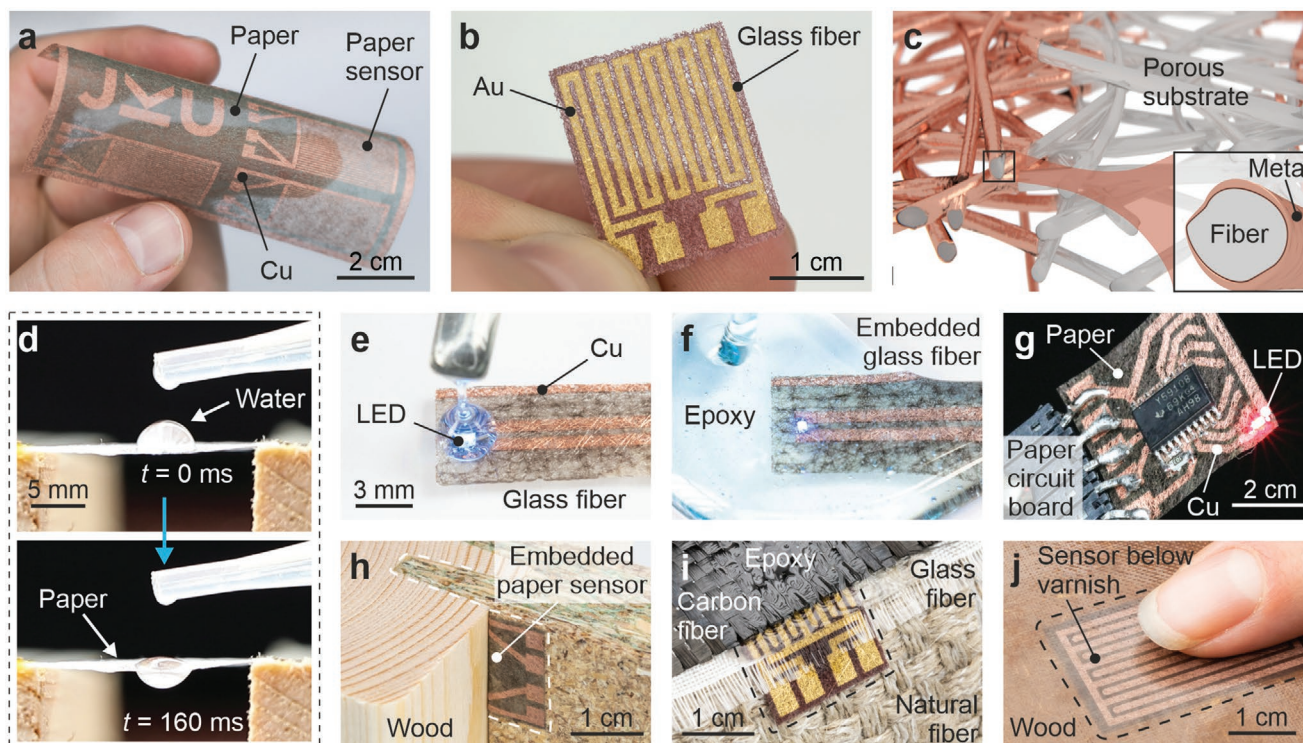


Figure 1. iSens on porous substrates. a) Flexible impedance sensors consisting of interdigital electrodes (Cr/Cu) on a lightweight, permeable paper. b) Temperature sensor consisting of a meander electrode (Cr/Au) on a glass fiber fleece. c) Single-substrate fibers are fully coated with metal films (Cr/Cu, Cr/Au) to achieve high electrical conductance. d) The porosity of the paper is high enough for a drop of water to percolate through within 160 ms. e) An electrically functionalized glass fiber sheet with a connected LED. f) The system is fully functional when encased in epoxy. g) Electrical components are soldered onto the sensor substrates and create circuit boards including chips, connectors, and LEDs. h) Embedded sensors are used to monitor 3D wood-glue joints or fiber constructions (i). j) Underneath a transparent varnish, the sensor operates as a touch sensor.

The entire technology is non-destructive, operates in situ and in real-time, and is data compatible with the Internet of Things. Our iSens are fabricated by coating fibers with a metal to form individual and electrically conductive paths (Figure 1c). Although the substrates used (e.g., cellulose fiber papers) are lightweight and extremely permeable, allowing a drop of water to penetrate within 160 ms (Figure 1d), electrical components such as light-emitting diodes (LEDs) can be soldered onto them (Figure 1e) and then embedded in epoxy resin (Figure 1f). Several soldered connectors, a microchip, a resistor, and an LED show the possibility of complex circuits on the substrates (Figure 1g). Here, solder connections to a fiber substrate are superior to their counterparts on flat, non-porous substrates (i.e., flexible copper-coated printed circuit boards, PCB) because the solder does not attach to the surface only, but permeates and fills the fiber structure volume of the substrate around the soldering location. As a result, the solder is robustly connected and cannot be removed without rupture of the fibers and the entire system (Figure S1, Supporting Information). The paper sensors are highly flexible; repeated bending to radii of 6 mm for more than 2400 times leaves the conductivity of the metal traces nearly unchanged (<0.6% variation) and they even endure multiple “hard” folds (Section S1.4 and Figure S2, Supporting Information). This readily allows for insertion into 3D wood-glue joints (Figure 1h).^[16] Our glass fiber sensors do not act as defects in the fiber composite material and can be

integrated seamlessly (Figure 1i). The paper sensors are very thin and are also easily penetrated by a transparent varnish, which allows, for example, touch sensors to be realized on wooden surfaces (Figure 1j and Figure S3, Supporting Information). These enable wipeable and therefore germ-free electrical switches in medical areas.

2. Results and Discussion

Fabrication of the iSens comprises only three process steps. First, metal layers are thermally evaporated onto the front side of the porous substrate (Figure 2a). We used a 3 nm thick adhesive chromium (Cr)^[17] and a 300 nm conductive copper (Cu) or gold (Au) overlayer. The same metal layers are then evaporated onto the back to ensure optimal metallization of the fibers. Finally, custom sensor designs are realized by spatial laser ablation (Section S1.6 and Figure S4, Supporting Information). Due to fast temperature homogenization of the fibers, ablation from one side also removes the metal from the other side, thus drastically reducing fabrication complexity and processing time. We present two different substrate materials (Figure S5, Supporting Information) for different applications. An optical cleaning paper and a textile glass fiber. All sensor materials, parameters, and designs used throughout this work are listed in Table S1, Supporting Information. A 300 μm wide

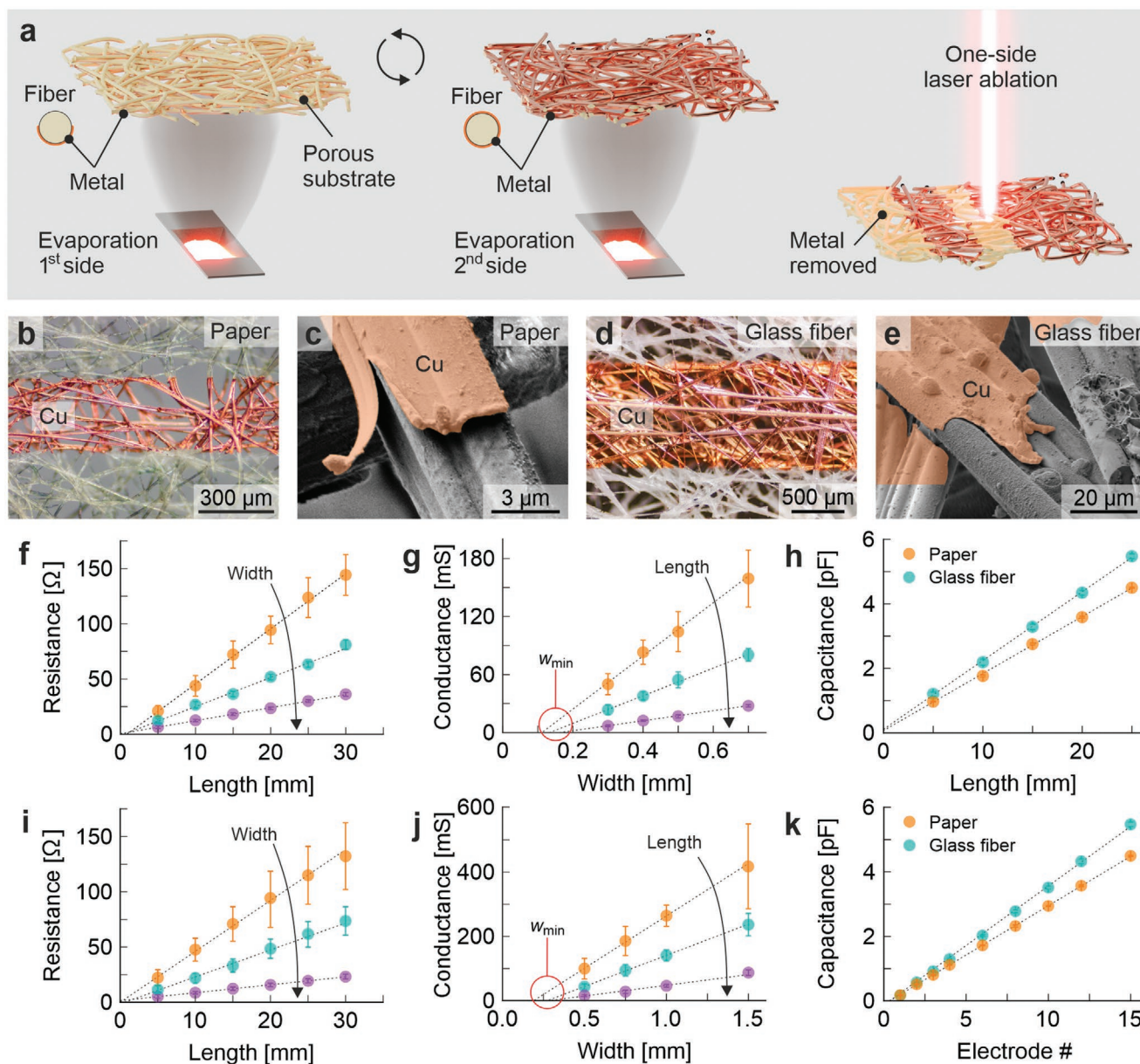


Figure 2. Fabrication steps for the electrodes with different geometries on porous substrates. a) Physical vapor deposition of the metal on the front side of the substrate, followed by rotation of the substrate and a second evaporation. The fibers are now fully coated with metal. In the final step, individual electrodes, or structures are created by laser ablation from one side only. b) Optical micrograph of a 300 μm wide electrode on paper and a 500 μm wide electrode on glass fiber (d). c) Scanning electron microscope (SEM) graphs of Cr/Cu coatings on paper fibers and glass fibers (e). The SEM pictures show the edge of a laser ablation. The dashed lines in graphs (f–k) are linear fits of the measured data. f) Resistance of an electrode as a function of length l for various widths w [0.3 mm (orange); 0.4 mm (turquoise); 0.7 mm (purple)] on paper and glass fiber (i) [0.5 mm (orange); 0.75 mm (turquoise); 1.5 mm (purple)]. g) Conductance of an electrode as a function of width w for various lengths l [5 mm (orange); 10 mm (turquoise); 30 mm (purple)] on paper and glass fiber (j). The intersection points of the linear fits with the x-axis indicate the minimum width w_{\min} for a functioning electrode. h) Capacitances of sensors on paper and glass fiber as functions of electrode length l and electrode number n (k).

Cr/Cu electrode on this paper is shown in Figure 2b,c. The Cu thickness of 300 nm provides sufficient conductivity for reproducible sensor behavior. Laser ablation yields clean edges, few residual copper particles, and little debris, thus avoiding short-circuiting between adjacent electrodes (300 μm gap). A 500 μm wide Cr/Cu electrode on the glass fiber is shown in Figure 2d,e. Again, a 300 nm-thick Cu layer provides sufficient conductivity.

Various measurements were carried out to find suitable electrode geometries. The resistance R of a Cr/Cu electrode of width w and length l (Figure S6a, Supporting Information, corresponding conductance $G = R^{-1}$) was measured by a 4-point scheme. We found a linear behavior ($R \propto l$, Pouillet's law) on paper (Figure 2f) and glass fiber (Figure 2i). Further, the conductance was linear in w (Figure 2g,j), but only above some

minimum width w_{\min} ($G \propto w - w_{\min}$). These data suggest that, for reliable electrical conductivity, an electrode should be at least 300 and 500 μm wide on paper and on glass fiber, respectively (for detailed information on geometry and error bars see Section S2, Supporting Information). On some substrates, the conductance also showed in-plane anisotropy (x or y , Figure S6b,c, Supporting Information). In accordance with the literature, the interdigital electrode (IDE) sensors (Figure S7a, Supporting Information) exhibited a linear increase in capacitance C with increasing electrode length l ($C \propto l$, Figure 2h).^[7,18] The capacity of the glass fiber sensors was slightly higher than that of the paper sensors due to substrate material properties (thickness, fiber density, and permittivity). Furthermore, there was an almost linear relation between the capacitance and the number of electrodes n ($C \propto n - 1$, Figure 2k). With one electrode (i.e., $n = 1$) parasitic capacitances during measurement were small. In summary, we have demonstrated that individual iSens can be created easily and simply on our permeable substrates. Note that the electrodes must be sufficiently wide to guarantee good functionality and conductance.

To understand the influence of paper substrate porosity on electrode functionality, we simulated both porous and solid electrodes using the finite element method (FEM). Two Cr/Cu electrodes on a paper substrate were read into CAD software from a 2D microscope image (Figure 3a) and then digitally extruded to imitate the 3D network structure. This porous model (Figure 3b) was compared to conventional interdigital electrodes (solid model, Figure 3c). In both CAD models the

electrodes were about 4.86 mm long, had width and spacing equal to 300 μm , and had a thickness h of 20 μm . The cross-sectional view of the normalized electrical potential distribution (similar to that in reference [19]) shows no noticeable difference between the two models (Figure 3d). The electric fields midway between the electrodes $E = E_x(x = 0, z)$ differs only slightly (Figure 3e). For the conventional electrodes (solid model), E_x is marginally higher for small z . The theoretical curve assumes a periodic set of infinitely thin solid electrodes ($h = 0$) with equal gap and width; see Equation (9)₃ in the Supporting Information, based on reference^[20] and references therein. It explains the results and the logarithmic slope of the FEM simulations; the field values are slightly lower than for FEM simulations with finite electrode thickness h . The charges, fields, and capacitance of the system increase with thickness h (about linearly for the capacitance) due to the presence of additional surfaces. However, the difference in capacitance between the porous and the solid structures remains small (Figure 3f). Here, the theoretical results again lie slightly below the simulated values, see Equation (12)₃ and (13)₄ in the Supporting Information, based on reference.^[21] Further physical implications and theoretical aspects of the fibrous structure of the paper sensors are also discussed in Section S1.5, Supporting Information.

In the production of wood-based composites, hot pressing is a commonly used process that is very energy-consuming and cost-intensive.^[22] For this reason, it is important to minimize both curing time and the amount of adhesive by optimizing the pressing conditions, such as temperature, pressure, and

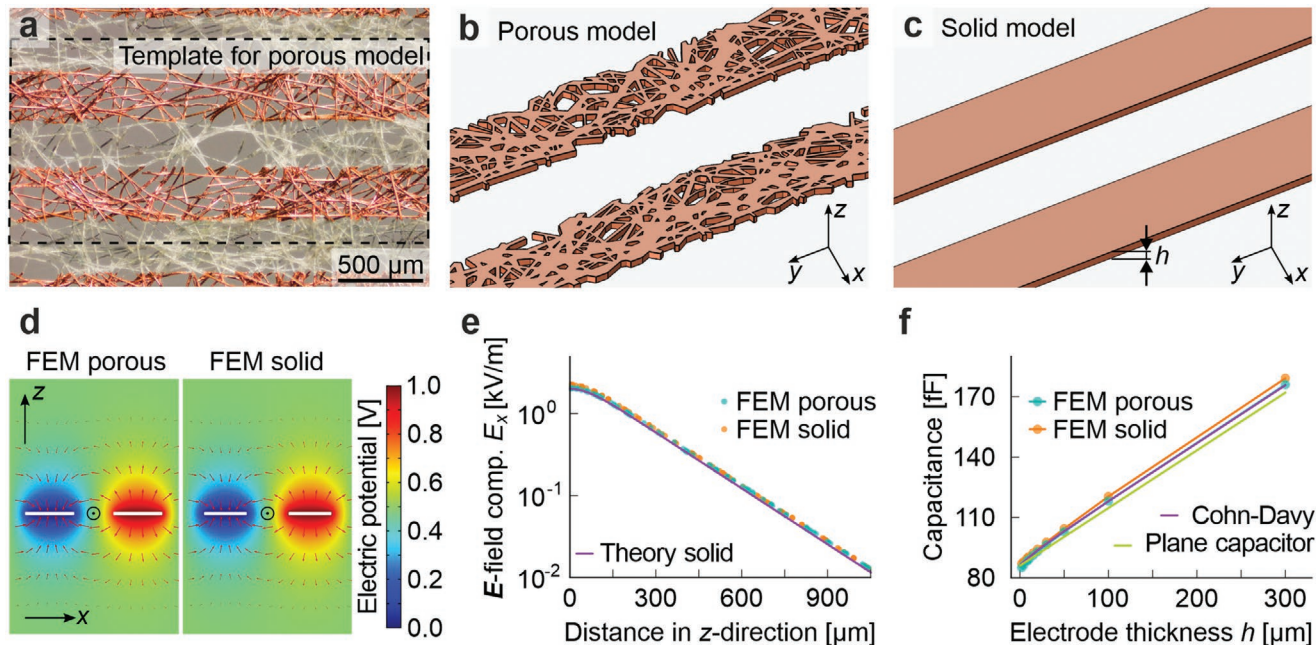


Figure 3. Structure and analysis of porous periodic interdigital electrodes ($w = g = 300 \mu\text{m}$), compared to conventional solid electrodes. a) Optical micrograph of the metalized paper electrodes. The dashed box shows the area used to create a FEM simulation model. b) Two electrodes are digitized and extruded in the CAD software to obtain the porous model with a thickness h of 20 μm . c) Solid model for conventional interdigital electrodes. d) FEM-simulated electrostatic potential for both models in air with potential difference $U = 1 \text{ V}$ between the electrodes, cross-sectional view. The small circle between the electrodes indicates the origin of the coordinate system and the y -direction used in other panels. e) The electric field at mid-gap $E = E_x(x = 0, z)$ decreases exponentially at large distances from the electrodes. The theoretical curve is for the infinite set of thin periodic electrodes with $h = 0 \mu\text{m}$, see Supporting Information Equation (9)₃. f) The capacitance increases approximately linearly with the electrode thickness h , see Supporting Information Equation (12)₃ and (13)₄.

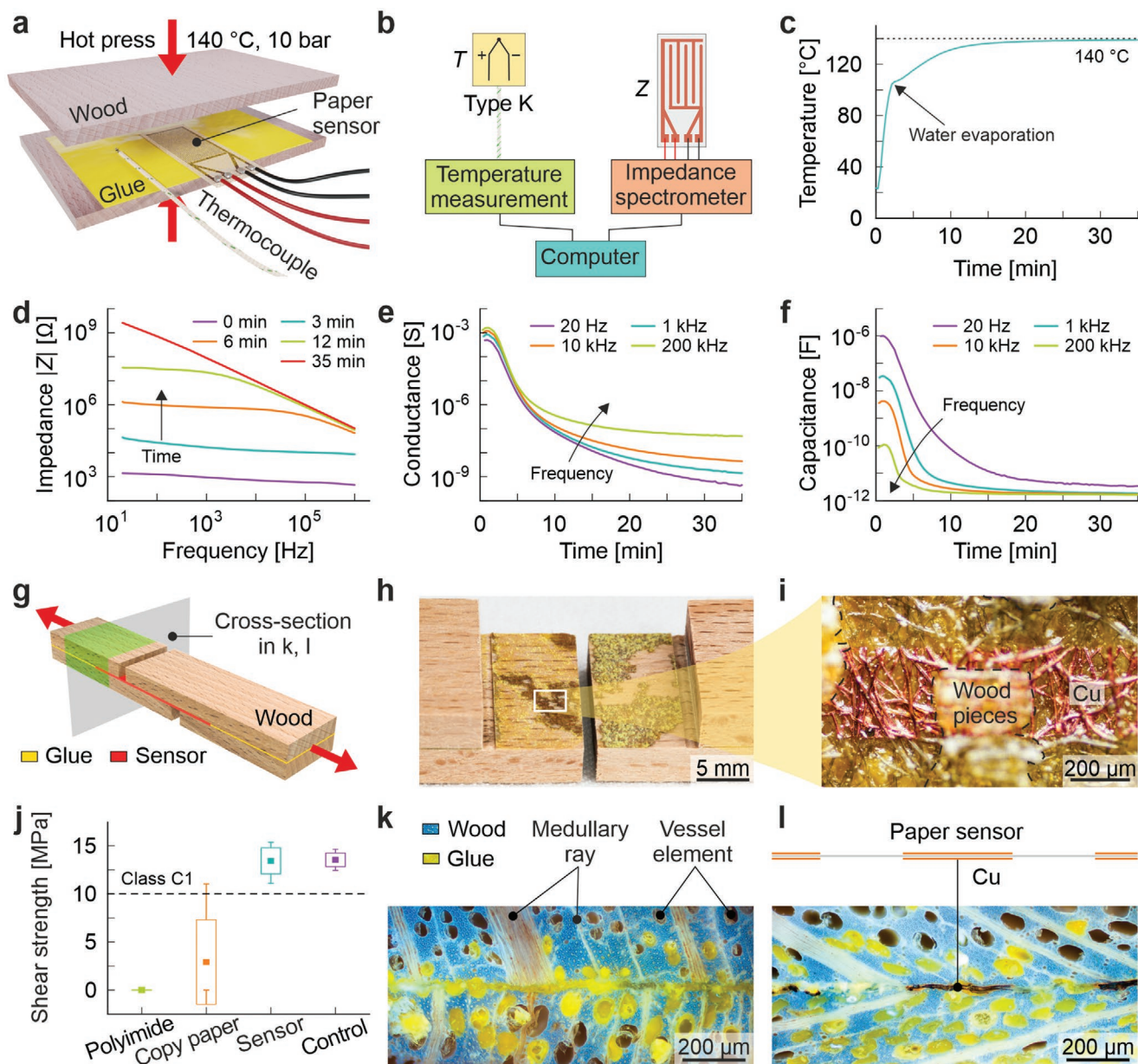


Figure 4. Paper sensor used to analyze the curing of wood glue and the influence of the iSen on the strength of the glue joint. a–b) Experimental setup for in situ investigation of the cross-linking reactions. c) Temperature of the glue joint inside the wood plates, measured by the thermocouple. d) Impedance, ohmic conductance (e), and capacitance (f) measured by the paper sensor at various frequencies. g) Tensile shear test sample in accordance with European standard DIN EN 205:2003. A paper sensor is glued in between the wood plates at the predefined breaking point. h) Wood sample, which is broken at the glue joint after the tensile test (WFP = 0%). The glued-in paper sensor remains attached to both wooden parts. i) The sensor is completely permeated by the yellow glue. Small pieces of wood remain attached due to the strong sensor-wood adhesion on both sides. j) Measured shear strengths of various materials in the glue joint. The quality class C1 lies above the dashed line (European standard DIN EN 12765-2001). k) Cross-section of a control wood sample (without a sensor) after the tensile test. l) Similar optical micrograph with an embedded paper sensor.

pressing time. In our case, it is a simple and practical method to put a flat and small IDE sensor between the wooden plates.^[6,23] For in situ investigation of the cross-linking reactions in wood glue, the sensor SenPZ1 was placed directly into the glue joint (Figure 4a). SenPZ1 is a sensor on a paper substrate that is used to measure the impedance Z (Table S1, Supporting Information). The boards were pressed together by a hot press at a stable temperature of 140 °C and a force of 10 kN

(corresponding to 10 bar in the glue joint). To verify, that glue can permeate the iSen, the adhesive was applied only to one side of the lower board. A thin type K thermocouple was inserted into the glue joint to monitor the temperature. The paper sensor response was measured with an impedance spectrometer. The spectrometer and thermocouple readings were fed into a computer for further processing (Figure 4b). At the beginning of the experiment, the wooden sample with the embedded sensors

was placed in the hot press, which closes completely in about 10 s. The time $t = 0$ in Figure 4c corresponds to the closed press and marks the beginning of the measurement. The heat diffused through the 5 mm thin beech wood into the glue joint, where the temperature reached 104 °C after 2 min. At this temperature, short-term temperature stabilization occurred. Evaporation of water is endothermic, which is reflected in a plateau in the curing temperature curves.^[24] Although the experiment was performed under atmospheric ambient pressure, the additional build-up of high pressure within small regions of the glue layer due to locally trapped water vapors^[25] increased the boiling temperature to above 100 °C. Similar experiments by Sernek et al. have shown that the plateau temperature increases when a warmer hot press is used.^[6] After the plateau, the temperature rose again and slowly stabilized at the hot press temperature of 140 °C. During the entire pressing time of 35 min, the impedance Z of the paper sensor within the glue joint was recorded (Figure 4d). Starting from a dominant resistive behavior over the whole frequency range (slope ≈ 0) at $t = 0$, the impedance changed to an almost ideal capacitive behavior (slope ≈ -1) at $t = 35$ min. Thus, it is reasonable to analyze these results within the framework of a parallel resistor-capacitor element (Section 1.7 and Figure S7b, Supporting Information). In the beginning, the glue was still liquid and provides high mobility for both electrons and ions. The mobile electrons cause a high ohmic conductance (Figure 4e), and the large amounts of highly mobile ions, results in electrode polarization, with high capacitance values, especially at low frequencies (Figure 4f).^[26] An increase in temperature first reduced the viscosity of the glue, and conductance and capacitance continued to rise slightly, reaching a maximum at about $t = 1$ min (Figure S7c, Supporting Information). At this point, the temperature was sufficiently high to induce cross-linking reactions within the glue, and mobility and number of ions decreased. As a result, conductance and capacitance then exhibited a trend reversal, and in the course of further cross-linking and water evaporation (drying), both values decreased. After 35 min the rate of change in the measured data was very small and the glue almost completely hardened. This experiment shows that the porous iSen presented here is suitable for continuous in situ monitoring of the curing process of wood glue in the manufacturing of wood-based composites. It withstands harsh conditions over the entire measurement period and delivers stable and reliable values that are comparable to those achieved with commercial sensors made of plastic^[6,27,28] or paper.^[16,23]

Presence of the embedded paper sensor should impair the bond strength of the glue joint as little as possible. To quantify its effect on the joint, tensile shear tests were performed (Figure 4g and Figure S8, Supporting Information). The wooden test samples with glued-in sensors were prepared and produced as in the previous hot-press experiment (pressure, temperature, amount of glue, etc.). In the center of the sample, both upper and lower wooden plates were notched to create a preferential breaking point at the sensor position. Every sample was pulled apart by a universal tensile testing machine until failure. The quality of a glue joint is characterized by the wood failure percentage (WFP), which is a visual estimation of the percentage of wood fibers covering the tested adhesive surface after the tensile test. For 8 samples, the wood broke completely

while the glue joint remained intact: an excellent WFP of 100% (Figure S8c, Supporting Information). Only one sample broke at the glue joint: a poor WFP of 0% (Figure 4h); only very small pieces of wood stuck to the sensor embedded in the yellow glue (Figure 4i). Thus, in the overwhelming majority of cases, and with a very high average WFP of 81%, the glue joint with the built-in sensor was stronger than the wood itself. The shear strength is the maximum shear stress $\tau = F/A$ before a sample breaks, where F is the applied load and A is the shear area ($10 \times 20 \text{ mm}^2$). We compared the tensile test results of our porous sensor with those of three additional material configurations. All measurement results are listed in Table S2, Supporting Information. Polyimide as a sensor substrate did not result in appreciable bonding and exhibited a WFP of 0% because the glue could not penetrate it (Figure 4j). Standard copy paper was also not suitable as a sensor substrate, because shear strength and WFP were too low and varied too widely. The adhesive joint without a sensor (control sample) achieved a very high shear strength of 13.5 MPa and an average WFP of 100%. This WFP value shows that the glue joint is stronger than the wood, and the shear strength characterizes the wood itself, rather than the glue. The measured shear strength of our porous sensor showed moderate standard deviation, and all values were above 10 MPa, which corresponds to quality class C1 according to European Standard DIN EN 12765-2001 and is within the range of values achieved without any sensor.^[29–31] After the tensile tests, the broken wood samples were cut to analyze the microscopic condition of the glue joint in a cross-section (Figure 4g). The adhesive joint was trimmed by microtome cuts and investigated with an optical microscope. For good contrast, fluorescence microscopy with appropriate filters was used, which showed the wood in blue color.^[32] The glue layer without a sensor was very thin (Figure 4k) and exhibited a glue distribution as seen in other papers.^[32,33] More vessels were filled with yellow glue in the lower board than in the upper one, probably because the glue was applied only to the lower plate before hot pressing. The glue joint with embedded sensor was equally thin and exhibited a similar glue distribution (Figure 4l). This is important because penetration of the glue into the wood is crucial for good adhesion.^[32] In previous work, we found that the porosity of conventional paper was not sufficient for the glue to permeate it,^[16] which is no longer the case for the improved porous paper sensor presented here.

In contrast to our paper sensor in wooden structures, our permeable glass fiber sensor is fabricated directly on the construction material, which makes it an additional, intelligent feature of the glass fiber itself. Dielectric analysis using IDE sensors is well suited for the characterization of adhesive curing.^[7] We chose Ag instead of Cu as the main electrode material to prevent oxidation during the high-temperature experiments (Figure S9a, Supporting Information). The experimental setup consisted of two glass fiber sensors (SenGZ1 and SenGR1, Table S1, Supporting Information) placed in a small molding frame (Figure 5a,b). SenGZ1 is an IDE sensor for measuring the impedance of the surrounding epoxy during curing (a process similar to the curing of wood glue). The smaller SenGR1 is a resistance sensor which monitors temperature changes after curing (Figure S9b, Supporting Information). A thin type K thermocouple was inserted into the frame to record

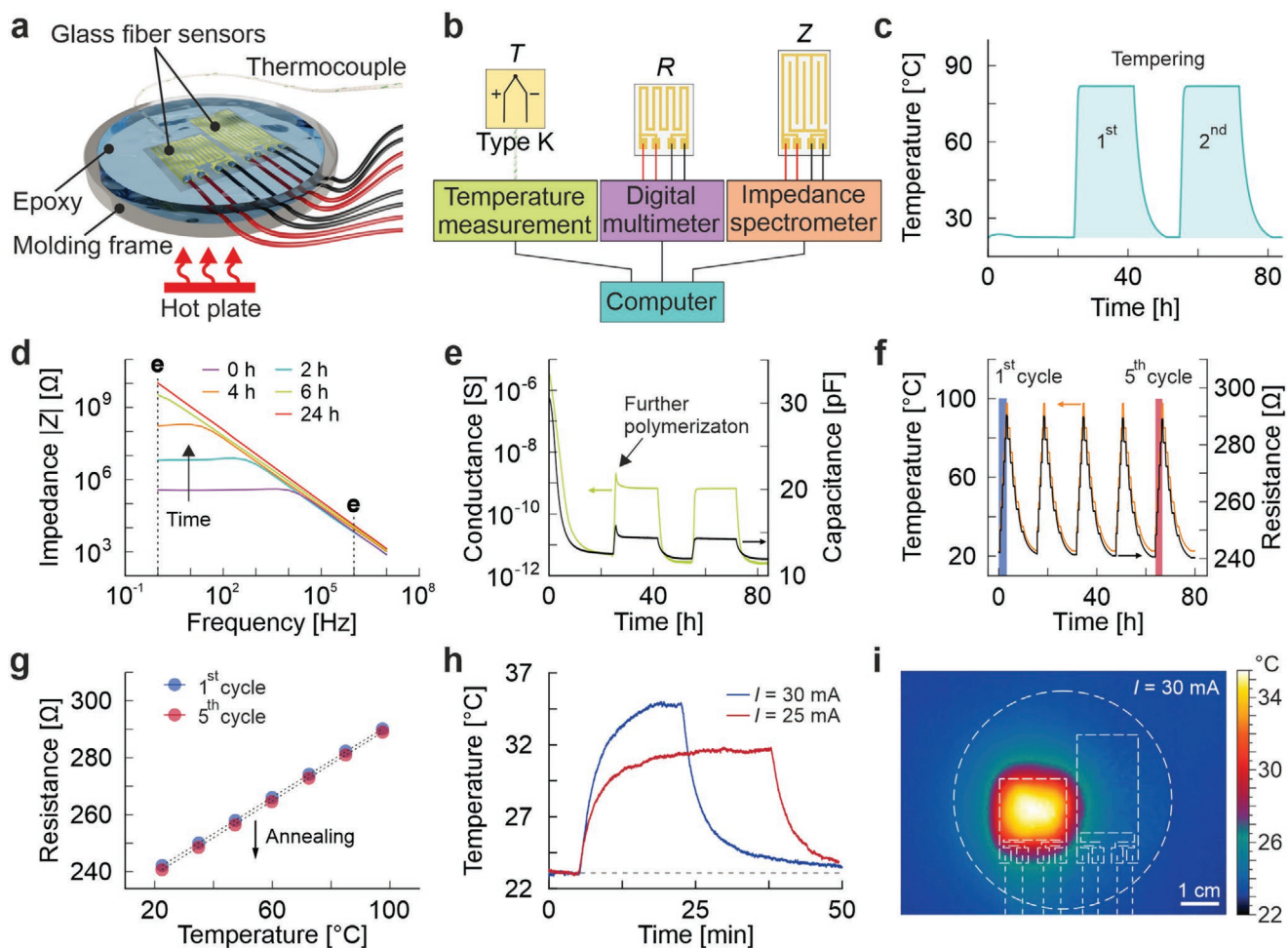


Figure 5. Glass fiber sensors used to analyze the curing of an epoxy resin and as a heater. a–b) Experimental setup for in situ investigations. c) Tempering profile generated by the hot plate and measured by the thermocouple. d) Impedance, conductance @ 1 Hz, and capacitance (e) @ 1 MHz measured by the glass fiber sensor SenGZ1. f) Temperature cycles after complete curing of the epoxy resin, measured simultaneously by the thermocouple and by SenGR1. g) Linear relationship between the temperature and the resistance of SenGR1. The sensor exhibits an annealing effect, shown here for the 5th cycle. h) SenGR1 is used to heat the surrounding epoxy by applying currents of 25 and 30 mA. Temperature is measured in the central region of the sensor with an IR camera. i) IR thermography image of the setup shown in (a) with an applied current of 30 mA through SenGR1. The dashed circle marks the molding frame, and other lines indicate the sensors and their cables.

the temperature. The entire experimental setup was placed on a hot plate to provide the heating necessary for tempering the epoxy. SenGZ1 was measured with an impedance spectrometer. In addition, a digital multimeter measured the resistance of SenGR1. The readouts from the spectrometer, the multimeter, and the thermocouple were sent to a computer for further processing. At the beginning of the experiment ($t = 0$), the mixed liquid epoxy was filled into the molding frame. Following the instructions from the datasheet of the epoxy system, it was cured for 24 h at 23 °C and then tempered twice for 15 h at 82 °C (Figure 5c). A small temperature increase (+1 °C) occurred in the first hours due to exothermic polymerization.^[34] The impedance Z measured by SenGZ1 showed a clear resistive behavior at lower frequencies (slope ≈ 0) during the first 4 h of measurement (Figure 5d). At higher frequencies, capacitive behavior (slope ≈ -1) was observed, which dominated across the whole frequency range after 6 h. Therefore, it was possible to apply the parallel resistor-capacitor model for these

results as well (Section S1.7 and Figure S7b, Supporting Information). Initially, the epoxy was liquid, and both conductance and capacitance were very high (Figure 5e and Figure S10a, Supporting Information). Due to progressive hardening in the first 24 h, both values decreased continuously. An increase in temperature during the first tempering caused conductivity and capacitance to rise again. The small peak at the beginning of the first tempering reflects a short hardening period of the epoxy (further polymerization), which did not occur during the second tempering. This confirms that the epoxy was almost completely cured already towards the end of the first tempering,^[34] where the values stabilize (see also curing kinetics in the Figure S10b,c, Supporting Information). If the temperature changes significantly afterward, the impedance just tracks these changes reversibly. These results demonstrate, that our glass fiber iSen is suitable for measuring and characterizing the curing of a commercial epoxy resin. It provides stable and reliable measurement data comparable to those from other

conventional sensors^[7,34] and can be used for in situ and real-time production monitoring. This intelligent glass fiber renders inserting an extra sensor—which may act as a foreign body in the composite—unnecessary.

The temperature sensor SenGR1 showed annealing effects during the first and second tempering processes,^[35] as reflected in a significant decrease in resistance at high temperatures (Figure S9c, Supporting Information). To characterize this behavior in detail, five cycles in which the temperature was varied from 23 to 98 °C were performed after curing of the epoxy (Figure 5f). The measured resistance followed the temperature, exhibiting a decrease of only 1.6 Ω (0.66%) from the initial value to the end of the fifth cycle, which are both at 23 °C. Figure 5g plots the resistance as a function of temperature for the first and fifth cycle, where linear behavior^[36] and the corresponding annealing effect can be seen. In each cycle, measurements were taken midway through each temperature step (i.e., when half the holding time had elapsed; see Figure S9d, Supporting Information). To finalize the sensor for the applications, the effect of annealing must be neutralized by long enough tempering before use. The linear behavior of the resistance makes this sensor suitable for temperature monitoring. Temperature sensors manufactured as thin-film metallic meanders can also be used as Joule heating elements in medical applications.^[37] In our case, the temperature sensor SenGR1 can heat the surrounding epoxy, for instance, to accelerate the curing or simulate local inhomogeneities. According to the data sheet, the gel time is halved if the temperature of the epoxy increases from 23 to 40 °C. A constant current of 25 mA applied to the sensor heats it to 31.5 °C (Figure 5h). A higher current of 30 mA further increases the temperature to 35 °C, as measured by an infrared (IR) camera (Figure 5i).

3. Conclusion

We have presented a simple and straightforward method for producing permeable sensors on flexible and porous substrates (paper and glass fiber). Fabrication includes physical vapor deposition and laser ablation. Conveniently, removal of the electrode materials can be achieved by laser ablation from only one side. The electrodes thus created should be sufficiently wide to ensure good functionality and conductance. Soldering various electrical components onto the sensor substrates and creating circuit boards is also possible. Theoretical and FEM analyses found only very small differences between conventional solid and porous electrodes. We have demonstrated that our paper sensor can withstand harsh conditions (140 °C, 10 bar) during hot-pressing of wooden constructions and provides data on the glue curing. The adhesive joint with the built-in paper sensor exhibited high mechanical stability. The glass fiber sensor, which is directly evaporated onto the construction material, provided stable data for epoxy curing during high-temperature phases. The characteristics of the resistance sensor make it suitable for use as a temperature sensor and as a heating element. We believe that our iSens platform will contribute to a new generation of flexible, permeable, and imperceptible sensors seamlessly integrated into various smart composite materials, further increasing their functionality in a wide variety of

applications, from automotive and construction industries to renewable energy production and healthcare.

4. Experimental Section

Paper substrate: Thorlabs Premium Optical Cleaning Tissue with a size of 124 × 73 mm², a thickness of 49 μm, and a grammage of 9.39 g m⁻². Its organic fibers, which are free from contaminants and adhesives, have a diameter of about 5–15 μm, and the wide-meshed fabric guarantees good permeability for liquids. This tissue meets the U.S. Government Lens Tissue Specification A-A-50177B.

Glass Fiber Substrate: Johns Manville Glass Fiber Nonwoven type FH 0.30/50 with a size of 210 × 297 mm² (DIN A4), a thickness of 0.32 mm, and a grammage of 48 g m⁻². The fibers are 8 μm in diameter, have random orientations, and are bonded together with a urea-formaldehyde resin.

Thermal Evaporation Materials: All metals were evaporated at a rate of 0.3 nm s⁻¹ and at a pressure below 0.8 mPa in a vacuum chamber. Cr: Kurt J. Lesker Chrome-Plated Tungsten Rods EVSCRW1 (0.07" diameter, 2" long, 99.9% purity). Cu: Kurt J. Lesker Copper Pellets EVMCU40EXQ (1/8" diameter, 1/4" long, 99.99% purity). Ag: Ögussa Fine gold granulate (99.98% purity).

Laser Ablation: A Trotec Speedy 300 laser engraver was used together with a fiber laser and a 2.85" lens.

Permeability Measurements: To visualize the high permeability of the paper-based sensor, a video was recorded with a frame rate of 50 Hz. The time between the deposition of the water droplet onto the sensor and complete droplet seepage to the opposite side was found from the frame by frame analysis and is about 160 ms (Figure 1d). This time gives an upper limit for the water permeation time, the wetting of the sensor region occurs faster. In addition, electrical measurements were made with an experimental setup similar to the one described in reference^[23] and found permeation times for wood glue-paper to be <1 s, water-glass fiber to be <2 s, and viscous epoxy resin-glass fiber less than 6 s. In practical application, the time scale relevant for permeability analysis and monitoring is typically significantly larger than these values.

Soldering on Porous Substrates: A standard non-RoHS solder was used (Sn60Pb39Cu1, RS Components) for soldering the electronic components (e.g., LED Driver: TLC59116IPWR Texas Instruments and Red LEDs: 150040RS73240, Würth Elektronik) onto the porous substrates (Figure 1e–g). Direct contact between substrates and the soldering iron was avoided by prior application of the solder to the contact pads of the components. The components were then positioned and soldered onto the substrate by tipping the contact pads with a flux fluid (428 532, Multicore) and heating the pads with the soldering iron (300 °C). In addition, low-temperature soldering was also performed (solder IND:282, indium corporation).

Touch sensor under transparent varnish: The medium-density fiberboard used had a thickness of 18 mm, a size of 10 × 10 cm², and was dried and conditioned at 23 °C and 50% rH for seven days before the experiment. The fiberboard, the paper sensor SenPZ2 (Table S1, Supporting Information) and 1.34 g of the powder coating (Drylac Wood Series 530, TIGER Coatings GmbH & Co. KG) were pressed together for 15 min by a hot press (LabEcon 300 Fontijne Presses) at a stable temperature of 150 °C and a force of 5 kN. This resulted in a pressure of 5 bar (0.5 MPa) and a desired powder application of 134 g m⁻². The capacitance of the paper sensor was measured with an impedance spectrometer at 1 MHz and a signal voltage of 2 V.

Scanning Electron Microscope (SEM) pictures: Measurements were taken using a Zeiss CrossBeam 1540 XB SEM at 3 keV acceleration voltage. Samples were prepared by thermally evaporating (0.1–0.5 nm s⁻¹, 1 × 10⁻⁹ bar) about 20 nm Cu, which provides good contrast in the SEM pictures.

Microscope Pictures: The optical microscope images were produced with a Nikon Industrial Microscope ECLIPSE LV100ND, a Zeiss Axioplan 2 Universal Microscope, and a KEYENCE VHX-7000 Digital Microscope.

Resistance and Impedance Measurements: Resistance and impedance of the electrodes and sensors were measured in 4-wire sensing mode by a Keithley 2110 Digital Multimeter, a Novocontrol Alpha-A, or an HP4284a impedance spectrometer.

Hot Press Experiment: The experiment was realized with a VOGT LaboPress P200T. The beech wood boards used (*Fagus sylvatica* L.) were 5 mm thick, $8 \times 12.5 \text{ cm}^2$ in size, and were dried and conditioned at 23 °C and 50% rH for seven days before the experiment. Before measurement, the lower beech board was covered with 3.05 g glue, which corresponds to the desired solid resin application of 200 g m^{-2} . The adhesive used was a mixture consisting mainly of an industrial urea-formaldehyde resin in combination with a formic-acid-based hardener. The solid resin content in the glue was 65.5 wt%, the water content 30.9 wt%, and the hardener content 3.6 wt%. The impedance was measured at frequencies ranging from 20 Hz to 1 MHz and a signal voltage of 1 V.

Tensile Shear Tests: The tests follow the European Standard DIN EN 205:2003 ("Determination of bond strength"). The samples have a size of $10 \times 20 \times 150 \text{ mm}^3$. Every sample was pulled apart at a controlled displacement rate of 1 mm min^{-1} by a Messphysik BETA 20/10 universal tensile testing machine. The actual displacement was measured with an optical sensor, using adhesive strips attached directly to the samples. At least 12 specimens of each type of sample were failure-tested. Kapton 300 HN 75 μm was used as polyimide and Multi Office Stress Free Paper (The Navigator Company) with a grammage of 80 g m^{-2} as standard copy paper.

Epoxy Curing Experiment: The molding frame is made of acrylic glass, with a height of 4 mm and an inner diameter of 5.7 cm. The epoxy system was composed of a commercial resin (Hexion Epoxy Resin MGS L 285) and a hardener (Hexion Hardener 285) at a weight ratio of 100:40. To create the epoxy, both components were mixed and degassed in a speed mixer. Once heat-treated, it is approved for use in the construction of aircraft, such as gliders and motorized planes (German Federal Aviation Authority), and is also used in scientific research.^[38] The impedance was measured at frequencies ranging from 1 Hz to 10 MHz and a signal voltage of 1 V.

Heating application: The current source for the heating experiments was a Keithley 2612 SYSTEM SourceMeter. The IR thermography images (resolution $320 \times 240, \pm 2 \text{ }^\circ\text{C}$) were taken by a FLIR 325sc IR camera.

Finite element simulation: The commercial FEM software COMSOL Multiphysics was used with the Electrostatic module to simulate the electrical properties of the sensors. Two models were built: one porous and one solid. These models included air and copper as main materials. The relative permeability of air is 1, and copper is considered to be an ideal conductor. Both models featured two electrodes, each one 300 μm wide and about 4.86 mm long (Figure 3b,c). The distance between them was 300 μm . The height of the computational domain in air was at least 1000 μm from the surface of the conductor, the width was 1200 μm and the length was the same as that of the electrodes. In the porous model, the shape of the electrodes was projected from the real sensor (Figure 3a) and extruded to a given thicknesses h in the z-direction. The periodic boundary conditions were used in the x- and y-direction and zero field conditions at the z-boundaries, which is justified for the overall neutral structure and large enough computational domain. In the simulations, a 1 V voltage was applied to the sensor to calculate the capacitance and analyze the distribution of the potential between the electrodes.

Supporting Information

Supporting Information is available from the Wiley Online Library or from the author.

Acknowledgements

This work was supported by the European Research Council Starting Grant "GEL-SYS" under grant agreement no. 757931, by the Austrian Research Promotion Agency GmbH (FFG) within the COMET project

TextileUX under grant agreement no. 865791, and within the Austrian Research Promotion Agency GmbH (FFG) BRIDGE Project "Interactive Wood" under grant agreement no. 874770. The authors dedicate this work to Siegfried Bauer.

Conflict of Interest

T.S., and D.W. are cofounders of sendance, a start-up company developing sensor systems. T.S., U.M., R.S., and M.K. are listed as inventors on an Austrian patent application (AT523450) that describes a permeable electrode for sensor applications.

Author Contributions

T.S., U.M., R.S., S.B., and M.K. conceived the research project; T.S. prepared the materials with input from M.S. and F.E.; T.S. fabricated the sensors, conducted the experiments and analyzed the data; S.D. recorded the SEM images; R.P. soldered the electronic components; G.M. conducted the FEM simulation; N.A. developed the theoretical models; T.S., D.W., and M.D. designed the figures; T.S., D.W., N.A., and M.K. wrote the manuscript; all authors contributed to editing the manuscript; M.K. gave input at all stages and supervised the research.

Data Availability Statement

The data that support the findings of this study are available from the corresponding author upon reasonable request.

Keywords

glass fibers, laser ablation, papers, porous materials, sensors

Received: April 10, 2021

Revised: May 24, 2021

Published online: August 2, 2021

- [1] D. Marikyan, S. Papagiannidis, E. Alamanos, *Technological Forecasting and Social Change* **2019**, 138, 139.
- [2] P. Mohankumar, J. Ajayan, R. Yasodharan, P. Devendran, R. Sambasivam, *Measurement* **2019**, 140, 305.
- [3] M. E. Mott, J. O. Wobbrock, In *Proc. of the 2019 CHI Conf. on Human Factors in Computing Systems*, Association for Computing Machinery, New York **2019**.
- [4] G. Churkina, A. Organschi, C. P. O. Reyer, A. Ruff, K. Vinke, Z. Liu, B. K. Reck, T. E. Graedel, H. J. Schellnhuber, *Nat. Sustain.* **2020**, 3, 269.
- [5] S. Prashanth, K. Subbaya, K. Nithin, S. Sachhidananda, *J. Mater. Sci. Eng.* **2017**, 6, 1000341.
- [6] M. Sernek, F. A. Kamke, *Int. J. Adhes. Adhes.* **2007**, 27, 562.
- [7] Y. Yang, G. Chiesura, T. Vervust, F. Bossuyt, G. Luyckx, J. Degrieck, J. Vanfleteren, *Sens. Actuators, A* **2016**, 243, 103.
- [8] P. Palma, R. Steiger, *Constr. Build. Mater.* **2020**, 248, 118528.
- [9] M. Riggio, M. Dilmaghani, *Building Research & Information* **2019**, 48, 1.
- [10] R. Volk, J. Stengel, F. Schultmann, *Automation in Construction* **2014**, 38, 109.
- [11] W. Lang, F. Jakobs, E. Tolstosheeva, H. Sturm, A. Ibragimov, A. Kesel, D. Lehmhus, U. Dicke, *Sens. Actuators, A* **2011**, 171, 3.
- [12] F. Güder, A. Ainla, J. Redston, B. Mosadegh, A. Glavan, T. J. Martin, G. M. Whitesides, *Angew. Chem., Int. Ed.* **2016**, 55, 5727.

- [13] K. Alkin, T. Stockinger, M. Zirkl, B. Stadlober, S. Bauer-Gogonea, M. Kaltenbrunner, S. Bauer, U. Müller, R. Schwödiauer, *Flexible Printed Electron.* **2017**, 2, 014005.
- [14] A. Miyamoto, S. Lee, N. F. Cooray, S. Lee, M. Mori, N. Matsuhisa, H. Jin, L. Yoda, T. Yokota, A. Itoh, M. Sekino, H. Kawasaki, T. Ebihara, M. Amagai, T. Someya, *Nat. Nanotechnol.* **2017**, 12, 907.
- [15] Y. Wang, S. Lee, T. Yokota, H. Wang, Z. Jiang, J. Wang, M. Koizumi, T. Someya, *Sci. Adv.* **2020**, 6, eabb7043.
- [16] T. Stockinger, R. Moser, U. Müller, F. Padinger, S. Bauer-Gogonea, S. Bauer, R. Schwödiauer, presented at *19. ITG/GMA-Fachtagung*, Nürnberg, Germany, June **2018**.
- [17] H. Aouani, J. Wenger, D. Gérard, H. Rigneault, E. Devaux, T. Ebbesen, F. Mahdavi, T. Xu, S. Blair, *ACS Nano* **2009**, 3, 2043.
- [18] R. Igreja, C. J. Dias, *Sens. Actuators, A* **2004**, 112, 291.
- [19] Y. Yang, G. Chiesura, T. Vervust, J. Degrieck, J. Vanfleteren, *J. Polym. Sci., Part B: Polym. Phys.* **2016**, 54, 2028.
- [20] E. Danicki, Y. Tasinkevych, *Sensors* **2012**, 12, 11946.
- [21] S. B. COHN, *IRE Trans. Microwave Theory Tech.* **1960**, 8, 638.
- [22] C. Gonçalves, J. Pereira, N. T. Paiva, J. M. Ferra, J. Martins, F. D. Magalhães, A. Barros-Timmons, L. Carvalho, *Eur. J. Wood Wood Prod.* **2020**, 78, 333.
- [23] T. Stockinger, B. Liedl, M. Steiner, R. Schwödiauer, F. Padinger, S. Bauer, M. Kaltenbrunner, U. Müller, *Sens. Actuators, B* **2020**, 324, 128750.
- [24] M. Kariz, M. Jost, M. Sernek, *Wood Res.* **2009**, 54, 41.
- [25] P. García, S. Wang, *Wood Fiber Sci.* **2005**, 37, 691.
- [26] R. J. Klein, S. Zhang, S. Dou, B. H. Jones, R. H. Colby, J. Runt, *J. Chem. Phys.* **2006**, 124, 144903.
- [27] M. Jost, M. Sernek, *Wood Sci. Technol.* **2009**, 43, 153.
- [28] U. Müller, C. Pretschuh, R. Mitter, S. Knappe, *Int. J. Adhes. Adhes.* **2017**, 73, 45.
- [29] E. Bachtiar, G. Clerc, A. Brunner, M. Kaliske, P. Niemz, *Holzforschung* **2017**, 71, 391.
- [30] S. Clauß, M. Joscak, P. Niemz, *Eur. J. Wood Wood Prod.* **2011**, 69, 101.
- [31] P. Hass, C. Müller, S. Clauss, P. Niemz, *Wood Mater. Sci. Eng.* **2009**, 4, 140.
- [32] F. A. Kamke, J. N. Lee, *Wood Fiber Sci.* **2007**, 39, 205.
- [33] P. Hass, F. K. Wittel, M. Mendoza, H. J. Herrmann, P. Niemz, *Wood Sci. Technol.* **2012**, 46, 243.
- [34] Y. Yang, G. Chiesura, G. Luyckx, T. Vervust, F. Bossuyt, M. Kaufmann, J. Degrieck, J. Vanfleteren, *Procedia Technology* **2014**, 15, 631.
- [35] A. P. Dorey, J. Knight, *Thin Solid Films* **1969**, 4, 445.
- [36] J. M. Heras, E. E. Mola, *Thin Solid Films* **1976**, 35, 75.
- [37] D. Wirthl, R. Pichler, M. Drack, G. Kettlguber, R. Moser, R. Gerstmayr, F. Hartmann, E. Bradt, R. Kaltseis, C. M. Siket, S. E. Schausberger, S. Hild, S. Bauer, M. Kaltenbrunner, *Sci. Adv.* **2017**, 3, e1700053.
- [38] C. Scarponi, M. Messano, *Composites, Part B* **2015**, 69, 542.

ADVANCED MATERIALS

Supporting Information

for *Adv. Mater.*, DOI: 10.1002/adma.202102736

iSens: A Fiber-Based, Highly Permeable and Imperceptible Sensor Design

*Thomas Stockinger, Daniela Wirthl, Guoyong Mao, Michael Drack, Roland Pruckner, Stepan Demchyshyn, Melanie Steiner, Florian Egger, Uwe Müller, Reinhard Schwödiauer, Siegfried Bauer, Nikita Arnold, and Martin Kaltenbrunner**

Supporting Information

iSens: A Fiber-Based, Highly Permeable and Imperceptible Sensor Design

*Thomas Stockinger, Daniela Wirthl, Guoyong Mao, Michael Drack, Roland Pruckner, Stepan Demchyshyn, Melanie Steiner, Florian Egger, Uwe Müller, Reinhard Schwödiauer, Siegfried Bauer, Nikita Arnold, and Martin Kaltenbrunner**

1. Theoretical considerations**1.1 Fields for the arbitrary finite system of parallel conducting strips**

Electrostatics of interdigital capacitors was analyzed in several works. Standard ref.^[1] analyses two adjacent electrodes within an infinite periodic sequence, or at the edge of a similar semi-infinite sequence using conformal mapping technique, and then combines them in parallel to obtain total capacitance. This approximation neglects the edge effects apart from the last pair of strips. We adopt a somewhat different approach, which (in principle) can provide exact compact expressions for the fields even for unequal electrodes, charges and voltages. It is inspired by the works,^[2-5] the refs. therein, and other works of these authors, which however do not provide the necessary expressions in a convenient form. Here, we mainly provide the physical explanations and the relevant final results, omitting the mathematical subtleties.

Let us first consider system of electrodes in vacuum. The potential φ is harmonic, and so, by differentiation are its gradient components, i.e., all components of the electric field $\mathbf{E} = (E_x, E_y) = -(\varphi_x, \varphi_y)$, or displacement \mathbf{D} . Here, $E_{x,y}$ denotes the components, while $\varphi_{x,y}$ the partial derivatives. For the planar 2D problems, due to $\text{div } \mathbf{E} = 0$, two Cartesian components satisfy Cauchy–Riemann conditions, and therefore can be combined into a single complex analytic function, for example $\Phi = E_y + iE_x$. If Φ satisfies boundary conditions on the electrodes and at infinity, it describes the field distribution everywhere. It is known and can be verified, that for a conducting half-plane $x > 0$, or a strip $-a < x < a$ the relevant functions are the appropriately chosen branches of the following expressions:

$$\Phi \stackrel{1}{\sim} \frac{c}{2\sqrt{z}} \quad \text{and} \quad \Phi \stackrel{2}{\sim} \frac{c}{\sqrt{a^2 - z^2}} \stackrel{3}{=} \frac{c}{\sqrt{-(z+a)(z-a)}} \quad (1)$$

Inspired by this expression, let us consider a system of n arbitrary metallic stripes on the x -axis, describes by the even array of their end points $a_1 \dots < a_j < \dots a_{2n}$, *ordered* from left to right in an ascending order. The appropriate function, with the rule of thumb for the branch choice for the strips with alternating charge is as follows:

$$\Phi = \underset{\text{normal}}{E_y} + i \underset{\text{tangential}}{E_x} \stackrel{2}{=} \frac{g(z)}{\sqrt{-\prod_j (z - a_j)}} \stackrel{3}{=} \frac{g(z)}{\exp[\frac{1}{2} \sum_j \ln |z - a_j| + \frac{i}{2} \{\pi + \sum_j \arg(z - a_j)\}]} \quad (2)$$

Here $-\pi < \arg < \pi$ is assumed for the arguments of complex multipliers. With this choice, the first stripe at the left is positively charged. For $z \rightarrow -\infty$, the expression under the root is negative, because the power $2n$ is even. Odd number of terms corresponds to a conductor extending to infinity at one of the sides of the system. In this case, or if the infinite conductor is present at both sides, the choice of the branch should be readjusted. The key is the switching between the purely real and imaginary parts on the opposite sides of the branching points $z = a_j$. The rule of thumb is, that the expression under the root should be *positive* on the metallic strips, and negative on the x -axis outside of them. Then, on the strips Φ has only the real part (i.e., *normal* field component, responsible for the charge density. Tentatively, the positive real root should be chosen on the positive strips, and negative on the negative ones), but no imaginary part (i.e., *tangential* field component, which makes the strip equipotential). Between the strips the situation is reversed – there is no charge, while the potential changes. The sign choice in Equation (1) and (2) satisfies these requirements. This framework does not explicitly discuss the potential. The stripes are equipotential, because $E_x = 0$ there.

Constant numerator c in Equation (1) is replaced in Equation (2) by an appropriate analytic function g , tentatively positive. This function is chosen to adjust the charges and/or mutual potentials between the strips. Therefore, $g(z)$ cannot grow faster than a polynomial of power $n-1$ (in the absence of an external field). Note, that 2D potential from a finite charge is logarithmic, while the fields decay as $1/z$. We implicitly use such a decay of fields at infinity. Within the linear electrostatics, if the appropriate function is found by some “guess”, it represents a correct and unique solution.

Here, $2n$ is the power of the polynomial under the square root (n is the number of strips and $2n$ the number of their edges). Polynomial of degree $n-1$ contains n coefficients. They should be determined from the given charges on the strips, proportional to the normal field integrals on

each strip, $Q_j \sim \int_{a_{j/2}}^{a_{j/2+1}} E_y dx$; or potentials between them, proportional to the tangential field

integrals between the strips: $U_{j/2}^{j/2-1} \sim \int_{a_{j/2-1}}^{a_{j/2}} E_x dx$. The resulting expressions contain analytically

unsolvable integrals, but are linear with respect to the coefficients of the polynomials. As a result, the corresponding numerical procedure reduces to the system of linear equations which can be solved very efficiently. In the more general cases, the function $g(z)$ can account for some externally imposed field, and the solution based on Equation (2) will represent the behavior of the charged conducting strips in such an external field, with the appropriate conditions at infinity. Examples of calculations *without* external field are shown in Figure S11a-f. The voltage differences are prescribed sequentially, starting from the 1st electrode, which is assumed to be positive. The *full* charges divided to the voltage difference correspond to the normalized SI capacitance from Equation (10) below, $2\epsilon L/L \mapsto 2$ in an ideal periodic case. The total charge is always 0 in all figures, because the polynomial $g(z)$ in the numerator of the

Equation (2) has degree $n-1$. This ensures the decay of the 2D fields at infinity, which is possible only for the overall neutrality of the system.

For reference and comparison purposes we provide the expression for the capacitance of two arbitrary *unequal* strips (with the opposite *equal* charges $\pm Q$) derived by this method.

This corresponds to a capacitance

$$C = \frac{1}{2\pi} \frac{L}{K(k_1)} \frac{K(k)}{K(k_1)} \stackrel{2}{=} 0.78 \frac{L}{2\pi} \quad (3)$$

Here L is the length of (infinite) strips perpendicular to the complex plane, and the elliptic integral arguments are:

$$k = \sqrt{\frac{w_2 w_1}{(w_2 + g)(w_1 + g)}} \stackrel{2}{=} \frac{w}{w + g} \stackrel{3}{=} \frac{1}{2}, \quad (4)$$

$$k_1 = \sqrt{\frac{g(w_1 + w_2 + g)}{(w_2 + g)(w_1 + g)}} \stackrel{5}{=} \frac{\sqrt{g(2w + g)}}{w + g} \stackrel{6}{=} \frac{\sqrt{3}}{2}$$

Here, the second equalities (4)_{2,5} refer to the equal strip widths $w_1 = w_2 = w$, and the last ones (4)_{3,6} refer to the often-employed geometry with the equal gap and width, $g = w$. Due to mirror charge argument, the symmetric expressions (4)_{2,5} with $w_1 = w_2$ and f.f., also describe a conducting strip perpendicular to a conducting wall, (with half of the voltage difference), and hold also the for conducting half-planes (infinitely wide strips).

The equal gap-width capacitance is provided by the last expression (3)₂, because for this case $K(\frac{1}{2}) / K(\frac{\sqrt{3}}{2}) = 0.78$. Interestingly, this ratio cannot be expressed via simpler functions or constants. Note, that the resulting capacitance is smaller than for a pair of strips in the infinite sequence below (Equation (7)₅), due to lower normal fields and charges near the outer edges of the isolated pair of strips.

We do not further discuss finite sets of unequal strips here, and move on to the infinite periodic system of strips.

1.2. Infinite periodic interdigital capacitor

1.2.1 Capacitance in vacuum in CGS

Let us formally consider the infinite product under the root in Equation (2)₂, or the corresponding sum of logarithms in Equation (2)₃. Clearly, the resulting function should be periodic on the real axis. The only periodic functions with no poles in the complex plane are trigonometric functions. Physical intuition suggests the following test function.

$$\Phi = \overset{1}{\underset{\text{normal}}{E_y}} + i \overset{2}{\underset{\text{tangential}}{E_x}} = \frac{c}{\sqrt{\cos \frac{kg}{2} - \cos kz}} \overset{3}{\underset{y=0}{=}} \frac{c}{\sqrt{\cos \frac{kg}{2} - \cos kx}} \quad (5)$$

Here and below $w/2$ and $g/2$ are half-width and half-gap of the stripe. The positively charged strip of width w lies from $g/2$ to $\lambda - g/2 = g/2 + w$, where $\lambda = g + w$ is the period of the cosine, and of the geometry of the stripes (but not of the potential), and $k = \frac{2\pi}{\lambda} = \frac{2\pi}{g + w}$. The

period of the potential of the whole structure is 2λ , due to alternating charges, which should be provided by the appropriate choice of the sign for the square root in Equation (5). L is the structure length in the 3rd dimension, which is assumed to be long enough (infinite), so that there is no appreciable dependence on the 3rd coordinate. The equipotential and field lines defined by the Equation (5) in the same way as for the finite system of stripes are shown in Figure S11g.

To find the potential between the adjacent stripes and their charges we choose the positive expressions under the square root for the corresponding field components, and use the formulas from the v.1 of ref.^[6] (1998 English CRC edition). We use CGS units and conventional notations for the Elliptic integrals and their arguments. In some references, for example in Mathematica software, these conventional arguments of the Elliptic functions should be squared, for example $K(\sin^2 \frac{kg}{4})$ should be used there, not $K(\sin \frac{kg}{4})$.

$$\begin{aligned}
 U &= c \int_{-g/2}^{g/2} \frac{dx}{\sqrt{\cos kx - \cos \frac{kg}{2}}} \stackrel{kx \rightarrow x}{=} \frac{2c}{k} \int_0^{\frac{kg}{2}} \frac{dx}{\sqrt{\cos x - \cos \frac{kg}{2}}} \stackrel{1.5.20.6}{=} \frac{2c}{k} \underbrace{\sqrt{\frac{2}{b}} F(\varphi, \frac{1}{\kappa})}_{\text{notations below}} = \frac{2\sqrt{2}c}{k} K(\sin \frac{kg}{4}) \\
 2\pi \frac{Q}{L} &= c \int_{g/2}^{\lambda-g/2} \frac{dx}{\sqrt{\cos \frac{kg}{2} - \cos kx}} \stackrel{kx \rightarrow \pi-x}{=} \frac{2c}{k} \int_0^{\frac{kg_1}{2}} \frac{dx}{\sqrt{-\cos \frac{kg_1}{2} + \cos x}} \stackrel{1.5.20.6}{=} \frac{2\sqrt{2}c}{k} K(\sin \frac{kg_1}{4}) \quad (6)
 \end{aligned}$$

in CRC notations: $\varphi = \arcsin \sqrt{\frac{b(1 - \cos x)}{a + b}} \mapsto \frac{\pi}{2}, \quad \kappa = \sqrt{\frac{2b}{a + b}} \mapsto \frac{1}{\sin \frac{kg}{4}}$

This leads to the following CGS capacitance per pair of strips:

$$C \stackrel{1}{=} \frac{Q}{U} \stackrel{2}{=} \frac{L}{2\pi} \frac{K(\sin \frac{\pi - kg/2}{2})}{K(\sin \frac{kg}{4})} \stackrel{3}{=} \frac{L}{2\pi} \frac{K(\cos \frac{\pi}{2} \frac{g}{g+w})}{K(\sin \frac{\pi}{2} \frac{g}{g+w})} \stackrel{4}{=} \frac{L}{2\pi} \frac{K(\sin \frac{\pi}{2} \frac{w}{g+w})}{K(\cos \frac{\pi}{2} \frac{w}{g+w})} \stackrel{5}{=} \frac{L}{2\pi} \quad (7)$$

Here, U is the *full* voltage between the electrodes (not a half-voltage). This result coincides with the formulas from ref.^[1] Expression (7)₅ assumes equal width and gap, $w = g$. In this case, the arguments of both elliptic integrals are the same, and the Elliptic integrals K cancel.

1.2.2 Dimensional fields at mid-gap and SI capacitance in dissimilar media

Using Equation (6) we can write the expression for the constant c in terms of potential U , or charge Q .

$$\begin{aligned}
 c &= \frac{kU}{2\sqrt{2}K(\sin \frac{kg}{4})} = \frac{\pi kQ/L}{\sqrt{2}K(\sin \frac{\pi - kg/2}{2})} \stackrel{\substack{g=w \\ \lambda=2w}}{=} \\
 &= \frac{\pi U}{2\sqrt{2}wK(\frac{\sqrt{2}}{2})} = \frac{\pi^2 Q/L}{\sqrt{2}wK(\frac{\sqrt{2}}{2})} = 0.6 \frac{U}{w} = 3.76 \frac{Q}{L} \quad (8)
 \end{aligned}$$

The second line here refers to equal gap and width, and in the last equality numerical values for this case are substituted.

Let us first obtain dimensional CGS fields at mid-gap $x=0$ using Equation (5). The cosine transforms into hyperbolic cosine, the expression under the square root is always negative, and we choose the natural branch, which corresponds to the positively charged first stripe to the right of $x=0$.

$$E_x = \text{Im} \left[\frac{c}{\sqrt{\cos \frac{kg}{2} - \cos kz}} \right] \stackrel{2}{=} \frac{c}{\sqrt{\cosh ky - \cos \frac{kg}{2}}} \stackrel{3}{=} \frac{c}{\sqrt{\cosh ky - \cos \frac{kg}{2}}} \quad \begin{matrix} x=0 \\ \cos kz \mapsto \cosh ky \end{matrix} \quad \begin{matrix} g=w, \lambda=2w \\ \frac{kg}{2} \mapsto \frac{\pi}{2} \end{matrix} \quad (9)$$

$$- \frac{\pi U}{2\sqrt{2}wK(\frac{\sqrt{2}}{2})\sqrt{\cosh \frac{\pi y}{w}}} \stackrel{4}{=} - \frac{\pi U e^{-\frac{\pi y}{2w}}}{2wK(\frac{\sqrt{2}}{2})} \stackrel{5}{=} - \frac{0.847U}{w} e^{-1.571\frac{y}{w}}$$

We provide the general expressions (9)_{1,2}, the mid-gap expression (9)₃ for equal width and gap $w = g$, as well as the exponential limiting expressions (9)_{4,5} far from the capacitor, at $y \gg w$. The expressions in SI in terms of voltage U remain the same, while the expressions in terms of charge Q should be modified using $U = Q / C$, where in vacuum C is multiplied by $4\pi\epsilon_0$, i.e., $Q \mapsto Q / 4\pi\epsilon_0$. In the case of homogeneous medium with the dielectric constant ϵ , or two half-spaces with ϵ_+, ϵ_- , the result in terms of *voltage* U still does not change, because the relation between the voltage and field is unaffected. The results with respect to *charge* Q change according to $Q \mapsto Q / 2\pi\epsilon_0(\epsilon_+ + \epsilon_-)$, and the displacement is calculated according to $D_{\pm} = \epsilon_0\epsilon_{\pm}E$. In particular, the SI capacitance with dissimilar materials on both sides of the strips becomes:

$$C \stackrel{1}{=} \epsilon_0(\epsilon_+ + \epsilon_-)L \frac{K(\sin \frac{\pi}{2} \frac{w}{g+w})}{K(\cos \frac{\pi}{2} \frac{w}{g+w})} \stackrel{2}{=} \epsilon_0(\epsilon_+ + \epsilon_-)L \quad (10)$$

The theoretical field, calculated using the expression (9)₃, is shown in Figure 3e by the solid magenta curve (Theory solid). It lies slightly lower than the numerical values for both solid and porous models. This is due to finite thickness contribution; if one simply multiplies the result (9)₃ by the “naive plane capacitor” factor $1 + h / g$ from the Equation (12) below, the agreement with the FEM calculations improves.

1.3. Thickness corrections for the capacitance

Comparison between the numerical and analytical capacitance (10) shows, that the numerical values are somewhat higher. This is mainly due to the finite thickness of the strips. For example,

in ref.^[7], the electrode thickness ($h = 5 + 100 \text{ nm}$ (Cr + Au), or less) is explicitly neglected in the capacitance ($w \sim g \sim 20\text{-}50 \text{ }\mu\text{m}$), but not the elastic part, see the text above Figure 4 there, and the last sections. Similarly, in ref.^[8] the electrode thickness $h = 10 + 40 \text{ nm}$ (Cr + Au) is mentioned, which is much less than period $\sim 200 \text{ }\mu\text{m}$, and the electrode thickness is neglected thereby. This is an essential difference to our case, which necessitates FEM calculations and thickness corrections performed in the current work. Various thickness corrections were suggested in the literature^[9-12] (see also ref.^[13]). All of them do not exactly correspond to our geometry, but produce reasonable values in the region of their applicability $h \ll w$. Our analysis indicates, that the best results over the wide range are given by the Cohn-Davy corrections, ref.^[14] based on ref.^[15] Somewhat less satisfactory (not shown) are the effective thickness corrections from Equation (6-7) in ref.^[16] and Equation (1) in ref.^[17]

1.3.1 Plane capacitor correction

The SI capacitance per pair of strips for infinitely thin plane case is given by the Equation (10). For very thick strip thickness h , the geometry between the strips becomes that of two $h/2$ -long plane capacitors with the plate separation g , connected in parallel, with dissimilar materials ϵ_{\pm} , which produces an additional capacitance:

$$C_{h \rightarrow \infty} = \frac{\epsilon_0(\epsilon_+ + \epsilon_-)hL}{2g} \quad (11)$$

In a periodic arrangement there are two such capacitors on both sides of each electrode. Thus, the lowest order approximation to the capacitance with strip thickness h is:

$$C \stackrel{1}{=} \epsilon_0(\epsilon_+ + \epsilon_-)L \left(\frac{K(\sin \frac{\pi}{2} \frac{w}{g+w})}{K(\cos \frac{\pi}{2} \frac{w}{g+w})} + \frac{h}{g} \right) \stackrel{2}{=} \epsilon_0(\epsilon_+ + \epsilon_-)L \left(1 + \frac{h}{g} \right) \stackrel{3}{=} 2\epsilon_0\epsilon L \left(1 + \frac{h}{g} \right) \quad (12)$$

The last expression assumes uniform material everywhere, $\varepsilon_+ = \varepsilon_- = \varepsilon$. The numerical results are still somewhat larger than this value, due to additional mutual capacitance between the perpendicular surfaces.

1.3.2 Influence of the edge effects

Cohn-Davy Equation (2-4) in ref.^[14] (based on ref.^[15]) provide the following results in our notations. We multiplied the edge contribution by 2, to account for both edges of the finger. The last expression (13)₄ below uses the limiting Equation (5) in ref.^[14], which holds for $h / g \geq 1$

$$k' = \sqrt{1-k^2}, \quad \frac{h}{g} = \frac{2 \frac{1+k^2}{2} K(k') - E(k')}{2E(k) - k'^2 K(k)} \quad (13)$$

$$\frac{C_h}{2\varepsilon_0 \varepsilon L} \approx 1 + \frac{2}{\pi} \ln \frac{E(k) - \frac{k^2}{2} K(k)}{\sqrt{k}} \approx 1 + \frac{h}{g} + \frac{2}{\pi} \left[1 + \ln \frac{\pi}{8} \right]_{0.0415}$$

The expressions (12) and (13)₃ are compared with the numerical FEM simulations of the solid model in Figure 3f, where they are shown as full curves “Plane capacitor” and “Cohn-Davy”, respectively. The numerical results are still marginally larger than the corrected values (13), due to *additional* mutual capacitances between the horizontal surfaces w and the perpendicular surfaces h , which are effectively connected in parallel. While the “plane capacitor” Equation (12) is purely linear in thickness, the Equation (13)₃ is sublinear at small h , reflecting edge effects in a plane capacitor of finite size.

1.4 Influence of bending onto the capacitance and resistance of the sensors

Small to moderate deformations lead to predictable changes in the sensor capacitance, and can be used to monitor the deformation of the host structure. In particular, cylindrical bending of the initially plane IDE (perpendicularly to fingers direction) into a curved one with radius B can be analyzed theoretically, using conformal mapping of the plane onto the exterior and

interior of a circle,^[7] or by the equivalent exponential-logarithmic change of variables

$\frac{z}{B} \leftrightarrow \zeta^{-1} \ln \frac{\rho}{B}$, where the ratio of periods $\zeta = \lambda_B / \lambda$ characterizes the stretching of the

electrodes on the reference cylinder. The latter approach works also for the layered substrates, even with the continues changes in $\varepsilon(z) \leftrightarrow \varepsilon(\rho)$. The planar capacitance C and the cylindrical capacitance C_B can be recalculated into each other as $C_B(h_{B,i}, \varepsilon_i, \dots) = C(h_i, \varepsilon_i, \dots)$, using rescaling of the planar layer thicknesses $h_i \leftrightarrow h_{B,i}$, outlined below.

Interestingly, in the homogeneous infinite surrounding, cylindrical bending does not modify its capacitance (per strip), which remains independent on the strip width (and therefore stretching ratio ζ). It depends only on the strip width/gap ratio, and is given by the expressions (7)_{3,4}, or (10) for the dissimilar media in SI units. For a single planar layer of thickness h , the equivalent cylindrical thickness h_R counted from the electrodes, positioned at $\rho = B$ is equal to:

$$h_B = \pm B(e^{\pm \frac{\zeta h}{B}} - 1) \approx \zeta h(1 \pm \frac{\zeta h}{2B}) \quad \Leftrightarrow \quad h = \pm \frac{B}{\zeta} \ln(1 \pm \frac{h_R}{B}) \approx \frac{h_R}{\zeta} (1 \mp \frac{h_R}{2B}) \quad (14)$$

Here, the upper/lower signs correspond to the layer on the outer/inner sides of the cylinder, and the last, 2nd order Taylor approximations assume small curvatures, or thin layers, so that $h/B \ll 1$. The expressions (14) imply, that (for thin layers, without stretching) the equivalent cylindrical layer should be thicker/thinner by a fraction $h/2B$ on the outer/inner sides of the reference electrode cylinder. For multilayer structures the thicknesses should be calculated similarly, considering the differences of the expressions (14) between the adjacent boundaries, counted from $z = 0$ and $\rho = B$, respectively; we omit detailed expressions for brevity.

The problem total resistance of the weakly conducting bulk material between the electrodes in the quasi-stationary homogeneous case is mathematically equivalent to the problem of capacitance for the same geometry, and can be analyzed in a similar fashion, with the result that

$$R = \varepsilon / 4\pi C \sigma = \varepsilon \varepsilon_0 / C \sigma, \quad \sigma \text{ being the electrical conductivity (Eq. (46.1) in v. 3 of ref. [18]).}$$

Thus, we do not expect appreciable change in resistance for small bending, which is confirmed by the experimental Figure S2a,b. For more general inhomogeneous cases, as a rule of thumb capacitance and resistance change in the opposite directions.

For large deformations, like a complete fold, analytic calculations are problematic, but one can perform an experimental tabulation, or numerical calculations. The details depend on the exact bending geometry, but as a rule of thumb the capacitance appreciably increases with folding due to the emergence/increase of mutual capacitance between various surfaces which become closer. The resistance decreases in a weakly conductive environment due to emergence of new conductance pathways, but can decrease if the electrode microstructure detrimentally changes upon many repetitions (many more than shown in Figure S2c) or in a complete “hard” fold (Figure S2d,e).

1.5. Corrections for the potentials and capacitance for the sensor with thin metallized fibers

1.5.1 Qualitative considerations

Though all metallized fibers have the same potential, the charges are distributed very unevenly between them (Figure S12a). Those in the middle are effectively screened “inside” the conductor, and bear almost no charge. Those along the perimeter are charged more, especially closer to the strip edges, as constant voltage results in a charge density singularity $\sigma \sim x^{-1/2}$ near the edge of a continuous conducting strip or a half plane, see Equation (1) for the normal component of the field E_y there. For fibers with the average radius a , and inter-fiber distance $l \gg a$, the potential homogenizes over the distances about l outside the strips.

For large distances $\rho \gg l$, the potential is defined by the *macroscopic* geometry of the system. Indeed, we can choose a surface at a distance about l from the surface of capacitor and apply the Gauss’s flux theorem for its interior. As $l \ll \lambda$, this does not noticeably alter the big picture.

Potential and fields outside such a Gaussian surface are fully determined by its macroscopic potential V_m , and are unaffected by the microscopic geometry inside. The total charge Q within such a surface is the same as for a continuous capacitor with the same macroscopic voltage V_m . These two quantities are related via the *macroscopic* capacitance C_m . For an interdigital capacitor with alternating strip voltages $\pm V_m$, strip width w , gap g , period $\lambda = 2(w + g)$, and two relevant rows of surface fibers on each side of the strip the overall macroscopic potential difference between the strips is:

$$U_m \stackrel{1}{=} 2V_m \stackrel{2}{=} \frac{Q}{C_m} \stackrel{3}{=} \frac{qw/l}{C_m(\epsilon, w/\lambda)}, \text{ with } q \stackrel{4}{=} \frac{Q}{w/l} \quad (15)$$

Here, the number of the appreciably charged peripheral fibers is w/l , and q is their average charge.

More accurately, there are *two* relevant layers of charged fibers in Equation (15) and (16), one on each side of the metalized paper strip. However, the microscopic logarithmic voltage increase occurs largely on the macroscopically external side of each of these layers, as the inner side is screened within the “bulk electrode”. One can think of a *single* layer of fibers (or wires) that was cut in two in the middle and pulled apart. Then, the normal component of the field and the corresponding surface charges are located predominantly only *on the outer half-cylinder of each surface fiber*. The inner half possesses practically no surface charges and no normal flux of the **D** or **E** field, because it is already inside the bulk of the “equipotential metallic network”. One can think of the surface connecting the middles of all cylindrical surface wires as being equipotential; nothing happens inside this surface. This equipotentiality is provided by the appropriate macroscopic *distribution of charges among all fibers*. Within this picture, it is more appropriate to use $q=Q/lw$, rather than $Q/2w$, as was done in the Equation (15) and (16).

However, V_m in the Equation (15) is not the *real* voltage applied to the thin metallized fibers of the electrodes. At small distances $a < \rho \ll l$ near each fiber, the potential undergoes an

additional logarithmic increase due to cylindrical nature of the potential there (Figure S12b). This increase is proportional to the fiber charge q , which via Equation (15) is related to Q and V_m . This leads to some general estimates, which we refine below, using a simple model problem.

1.5.2 Potential near the infinite periodic set of wires

Consider an infinite set of periodic equally charged linear wires in a host with the dielectric function ε (Figure S12c). If L is the dimension of the structure in 3rd direction, linear charge density on each fiber is q/L , and the *average macroscopic* surface charge density σ follows from Equation (15):

$$\sigma = \frac{q}{Ll} = \frac{Q}{wL}, \text{ with } q = \frac{Ql}{w} \quad (16)$$

The geometry resembles that of control (screening) grids in vacuum tubes and is discussed e.g., in ref.,^[19] with the potential given by the Equation (10.2.30) there. We use CGS here, and recalculate the result into SI when needed. Wherever possible, we use dimensionless ratios, which do not depend on the system of units.

$$V = \frac{q}{\varepsilon L} \text{Re}[-2 \ln(2 \sin \frac{\pi(x+iy)}{l})] = -\frac{q}{\varepsilon L} \ln 4(\sin^2 \frac{\pi x}{l} + \sinh^2 \frac{\pi y}{l}) \quad (17)$$

At large and small distances from each wire (e.g. for $x=0$) the expression (17)₂ yields:

$$V(y \rightarrow \infty) = -\frac{2\pi q|y|}{\varepsilon Ll} + O(e^{-\frac{2\pi|y|}{l}}) = -\frac{2\pi\sigma|y|^3}{\varepsilon} = V_\sigma \quad (18)$$

$$V(\rho \ll l) = \frac{2q}{\varepsilon L} \ln \frac{l}{2\pi\rho} + O(\frac{\rho^2}{l^2}) \stackrel{\rho=a}{=} \frac{2\sigma l}{\varepsilon} \ln \frac{l}{2\pi a} = V_a$$

Omitted terms in Equation (18)_{2,5} are small in terms of relevant dimensionless ratios. The expression (18)₂ corresponds to a potential of an equivalent plane with the homogeneous density σ . Its value at $V_\sigma(y=0)=0$ corresponds to a (shifted) macroscopic potential V_m in Equation (15). The lower expression in (18) is the *microscopic addition* to the fiber potential

V_{al} with respect to the macroscopic value. With the help of Equation (16), we express it via the overall strip charge Q , and further using Equation (15)₂ relate it to the macroscopic capacitance C_m (remember, that the overall macroscopic voltage $U_m = 2V_m$, see (15)₁):

$$V_{al} \stackrel{1}{=} \frac{2q}{\varepsilon L} \ln \frac{l}{2\pi a} \stackrel{2}{=} \frac{2Ql}{\varepsilon w L} \ln \frac{l}{2\pi a} \stackrel{3}{=} \frac{4V_m C_m l}{\varepsilon L w} \ln \frac{l}{2\pi a} \quad (19)$$

1.5.3 Capacitance modification due to fiber structure

Let us assume, that the overall charge Q is the same for both considered cases - macroscopic and fiber-based. In this case, the ratio of the true capacitance C , and the macroscopic one C_m , is equal to the inverted ratio of the true fiber voltages $V_a = V_m + V_{al}$ and its macroscopic part V_m :

$$\frac{C}{C_m} \stackrel{1}{=} \frac{V_m}{V_m + V_{al}} \stackrel{2}{=} \left(1 + \frac{4C_m l}{\varepsilon L w} \ln \frac{l}{2\pi a} \right)^{-1} \stackrel{3}{\approx} \left(1 + \frac{2l}{\pi w} \ln \frac{l}{2\pi a} \right)^{-1} \quad (20)$$

This is an estimate for the true capacitance C , which is smaller than the macroscopic value C_m , due to addition of the “idle” microscopic voltage V_{al} . The expression (20)₂ (written in CGS) is more general, while (20)₃ assumes equal strip width w and gap g , which implies expression (7)₅ for C_m , with the additional material factor ε . The overall macroscopic voltage on a capacitor is $2V_m$, so that C_m is the full capacitance per pair of strips (some authors use capacitance in one half-plane only). The dimensionless result (20) does not depend on the units used, and it does not even depend on the dielectric constant of the surrounding.

The numerical estimations for realistic values $l = 50\mu\text{m}$, $w = g = 300\mu\text{m}$, $a = 5\mu\text{m}$ result in $C = 0.95C_m$, or even $C = 0.8C_m$ if the value $l = 100\mu\text{m}$ from the Figure S12b,c is used. The expressions (20)_{2,3} are quite sensitive to l and a ; for example, the results for wire radius $a = 6.6\mu\text{m}$ (with other parameters kept the same) reproduce the ratio $C/C_m \approx 0.98$ obtained in numerical FEM calculation for the extrusion height $h = 20\mu\text{m}$. To better understand the

qualitative trends, we show the contour plot for the dependence of the ratio (20)₃ on l and a in the physical range of sizes in Figure S12d.

These estimations require at least $l > 2\pi a$, and for more reliable applicability $l \gg (2\pi)a$; they also implicitly contain additional subtle issues. The *effective* inter-fiber distance l at the surface is somewhat larger than in the bulk, as the non-surface fibers are effectively semi-screened. The homogenized Gaussian surface lies at a distance $\sim l$ outside of the surface fibers, which suggests the modification of the macroscopic geometry of the type: $w \mapsto w + 2l$, $g \mapsto g - 2l$, $h \mapsto h + 2l$. Also, the assumptions $a \ll l$, and, to some degree $h \ll w$, implied in correction (20), are not fully fulfilled for our numbers.

For our typical experimental numbers, the corrections are in the range of few percent only, but they are larger for thinner wires. These results should be used to compare capacitances of sensors with the same *macroscopic*, but different microscopic geometries – for example paper and glass sensors.

1.6 Copper removal mechanisms

There exist several mechanisms of laser material removal, which may become primary for various substrates and coating materials. Material is not always eliminated via the metal melting/evaporation, which require excessively high temperatures.^[20-23]

Let us first list the parameters of our laser system (Trotec Speedy 300), relevant for copper removal. It is an ytterbium pulsed fiber laser, with the wavelength $\lambda = 1.064 \mu\text{m}$, single pulse duration $\tau = 100 \text{ ns}$, operated at a repetition frequency $f = 20 \text{ kHz}$ and scanning velocity $v = 20 \text{ cm/s}$, with the focal spot diameter on the substrate $2w = 50 \mu\text{m}$. During one pulse the spot moves negligible $v\tau = 2 \times 10^{-2} \mu\text{m}$, and the inter-pulse displacement is $l = v/f = 10 \mu\text{m}$, which provides a reasonable overlap between the spots. The average laser power is $P = 3.4 \text{ W}$ for paper and $P = 6 \text{ W}$ for glass. This corresponds to single-pulse energies $E = P/f = 0.17 \text{ mJ}$

for paper, and $E = 0.3 \text{ mJ}$ for glass. The corresponding single-pulse fluence on the substrate is $\phi = E / \pi w^2 = 8.7 \text{ J/cm}^2$ for paper and $\phi = 15.3 \text{ J/cm}^2$ for glass. These high values result in single-shot material removal, as estimated below.

We use the following thermophysical parameters of paper and Cu^[22] in the subsequent estimations: vaporization and melting enthalpies: $\Delta H_v = 4.7 \text{ kJ/g}$, $\Delta H_m = 0.2 \text{ kJ/g}$, boiling and melting temperatures $T_b = 2567 \text{ }^\circ\text{C}$ (the real ablation temperature may differ), $T_m = 1084 \text{ }^\circ\text{C}$, density $\rho = 8.94 \text{ g/cm}^3$, specific heat $c = 0.4 \text{ J/gK}$, and thermal diffusivity $D = 1.12 \text{ cm}^2/\text{s}$.

This leads to the thermal diffusion length $l_T = 2\sqrt{D\tau} = 6.7 \text{ }\mu\text{m}$, which is much larger than the copper thickness of 300 nm and is comparable with the fiber diameter. As a result, the metal layer is almost homogeneously heated during the pulse even for one-sided irradiation. For the paper fiber material (bulk cellulose), we use density $\rho_p = 1.5 \text{ g/cm}^3$, specific heat $c_p = 1.336 \text{ J/gK}$, and thermal diffusivity $D_p = 0.01 \text{ cm}^2/\text{s}$. This leads to the much smaller thermal diffusion length $l_{T,p} = 2\sqrt{D_p\tau} = 0.63 \text{ }\mu\text{m}$, which implies that only the surface layer near the copper shell is strongly heated during the pulse.

The absorptivity of copper A is not well defined in such a system and is the main source of uncertainty. The complex refractive index of sputtered Cu at $\lambda \approx 1.064 \text{ }\mu\text{m}$ is about $n + i\kappa \approx 1.3 + i7.3$, which implies the optical penetration depth $l_\alpha \approx \lambda / 4\pi\kappa = 11.6 \text{ nm}$, i.e., the copper is optically thick. For the plane bulk copper the *normal* reflectivity is high for wavelength $\lambda > 0.7 \text{ }\mu\text{m}$, so that for $\lambda \approx 1.064 \text{ }\mu\text{m}$ $0.1 < A < 0.2$ was reported (it increases with temperature)^[24], see also refs.^[25, 26]. However, for the fibers with locally varying angle of incidence (absorptivity is higher for oblique incidence, but the local “area of incidence” is also larger), multiple reflections and inherent roughness the absorptivity can increase and easily vary in the range $0.1 < A < 0.3$ and beyond. We use $A = 0.2$ in the subsequent estimations.

The removal rate per pulse for pure vaporization can be estimated^[22] as $h = A\phi / \rho(\Delta H_v + \Delta H_m + cT_b)$, which results in $h \sim 328$ nm for paper and $h \sim 578$ nm for glass. Thus, a single pulse can *fully vaporize* the whole copper layer in both cases. We did not optimize the laser parameters and the pulse energy can probably be reduced in both cases, but the required energy remains significantly higher for glass.

The copper vaporization or even melting temperature is far above those of thermal decomposition or “burning” of paper, which lie in the range of 350–500 °C. However, we do not observe a destruction, alteration, or change in mechanical properties of paper upon copper removal from it (see Figure S4a). Neither do we observe visual traces of charcoal related to carbonization of cellulose, or changes in conductivity. We created two adjacent 30 mm long electrodes with a 50 μ m gap (smallest possible values for our laser engraving system, >300 μ m was used for the sensors). This ablated gap shows a very high resistance of 15.03 ± 0.94 G Ω , (measured with a Keithley 617 Programmable Electrometer). Such values are similar to those for pristine paper. The copper is also completely removed from both sides of the paper upon one-sided irradiation only. All these observations suggest, that the primary removal mechanism is different for the paper substrate. Most likely it is the explosive vaporization of water, and/or strong increase in pressure caused by the overheated water vapors and/or other volatile gaseous molecular fragments (e.g., CO, or CO₂)^[27] encapsulated inside the metallized fibers. Sharp increase in pressure, up to several hundred bars, occurs within tens of nanoseconds and exfoliates and removes the film without a significant (chemical) damage or alteration of the underlying fibers. Such film removal mechanisms may occur at lower laser fluences,^[28] at temperatures in the range of 100-300 °C, rather than 1100-2600+ °C, required for the melting/vaporization of copper. This mechanism is supported by the Figure 2c, where one can see almost no “droplet-like” debris, typical for the melting-evaporation mechanism.

Temperature estimations for such a complex structure can be only approximate. Apart from absorption uncertainty mentioned above, thinner fibers reach higher temperatures, which are about inversely proportional to the individual radius. Energy balance above shows, that the temperatures in the range 100-1000 °C are easily reached for the broad range of radii. The resulting pressures can be estimated from the Clapeyron-Clausius equation for the saturated vapors. Approximate sharp Arrhenius-type dependences for water (modified Back equation, based on ref.^[29]) and cellulose decomposition (Eq. (9) in ref.^[30]) result in pressures anywhere from 1 to $>10^4$ atmospheres, which makes the material removal based on vapor-driven exfoliation quite plausible. Low thermal diffusivity of cellulose ensures, that the possible thermal damage remains confined to the shallow heat affected zone near the fiber surface. Similar laser material removal mechanisms were successfully employed for laser cleaning of such sensitive and delicate substrates as textiles, medieval parchments and paintings.^[31, 32]

The situation is different for the glass substrates, where no humidity, or organic molecular fragments are trapped inside. At the same time, glass can sustain much higher temperatures (melting point of glass is 1400 to 1600 °C, depending on the composition, higher than 1084 °C for the copper). Besides, glass is not susceptible to chemical changes akin to carbonization, even upon fast re-solidification. Still, the ablation mechanism in this case is not necessarily based on evaporation. It can be driven by the thermal stresses, which build-up upon fast thermal expansion of the fiber and coating with strongly dissimilar (linear) thermal expansion coefficients (~ 0.5 ppm for glass, vs. 16.7 ppm for the copper). When the outer material has higher thermal expansion, the stationary thermal stresses are generally low, but the situation may be different for transient stresses. Figure 2e shows droplet-like debris, as well as structural alterations of the glass fibers in the ablated region. The one-sided removal worked a bit worse for glass substrates, and in the experiments we observed significant deterioration of the mechanical properties of the glass sensors upon ablation (see Figure S4b). The former observations hint towards the melting/evaporation mechanism, while the latter can be consistent

also with the stress-related one. It is difficult to pinpoint with certainty the ablation mechanism for the glass/copper system. However, high temperatures are less critical for the glass, as compared to paper, as long as the sensor largely sustains its structural integrity and can be incorporated into the desired structure, as in Figure S4c, which reveals only moderate deterioration of mechanical properties.

1.7 Impedance calculations (parallel resistor-capacitor model)

We characterize our system by the complex impedance Z (Figure S7b) with the real part Z_{re} and an imaginary part Z_{im} :

$$Z = Z_{re} + i \cdot Z_{im} \quad (21)$$

$$|Z| = \sqrt{Z_{re}^2 + Z_{im}^2} \quad (22)$$

Our impedance analyzers measure the impedance as a function of frequency f . Measured $Z_{im}(f)$ and $Z_{re}(f)$ dependences are analyzed within the simple parallel resistance-capacitance model (Figure S7b). Resistance R_p , capacitance C_p and conductance G_p are given by:

$$R_p = \frac{Z_{re}^2 + Z_{im}^2}{Z_{re}} \quad (23)$$

$$C_p = -\frac{Z_{im}}{Z_{re}^2 + Z_{im}^2} \cdot \frac{1}{2\pi f} \quad (24)$$

$$G_p = \frac{1}{R_p} \quad (25)$$

2. Electrode dimensions and resistance variation

Due to finite fiber density and sizes, the overall electrode dimensions (length and width) have a significant influence on the electrical resistance and conductivity. This is illustrated in Figures 2f,g,i,j which show the mean and standard deviation for 10 measurements.

Electrodes with a small width are markedly affected by the reduced number of cross-fiber junctions, which are responsible for the continuous conducting path along the fiber electrode. As the number of cross-fiber junctions decreases towards a critical value (current percolation threshold), the resistance of an electrode and the variation between the different samples increase strongly.

This effect is responsible for the larger error bars in Figure 2f,i obtained for the electrodes with the smallest width (orange data points). For similar reasons, higher conductivities and larger relative variations are observed for short electrodes, as compared to long electrodes, see Figure 2g,j.

3. Figures



Figure S1. Solder joint on the porous and highly flexible paper substrate. a) Twisted electrode with the operational built-in activated LED visualizes the high strength of the solder connections. b) Rear side of a solder joint, which shows that the solder permeates through the metallized paper fibers. c) iSens paper substrates with soldered wires typically rupture in the bulk when the applied tensile force exceeds the intrinsic fracture strength of the substrate, while the solder joints on both ends remain intact.

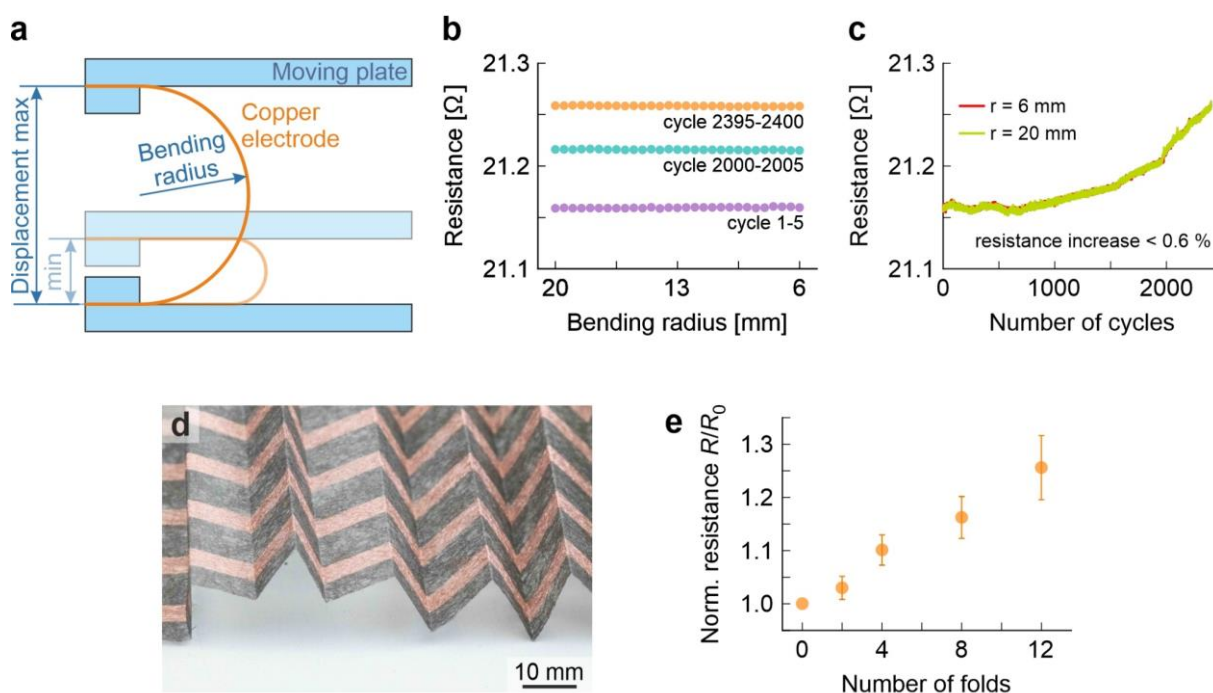


Figure S2. Bending and folding experiments with copper electrodes on the flexible paper substrate. a) Experimental setup for bending an 80 mm long (in the plane of the picture; 60 mm without clamps) and 3 mm wide electrode. Two plates bend the electrode to a bending radius between 20 mm and 6 mm. b) The resistance of the electrode was measured by a Keithley 2110

Digital Multimeter during 2400 bending cycles. The data points show the mean values for five sequential cycles. The bending itself shows no influence on the resistance value. c) The resistance after 2400 cycles increases by a small value of 0.6 %. d) Hard folded paper substrate with six copper electrodes with a length of 10 cm and a width of 2 mm. e) Measured resistance values (mean) increase slightly with more folds and show a moderate standard deviation. After twelve folds, an increase of resistance of ca. 25 % can be observed.

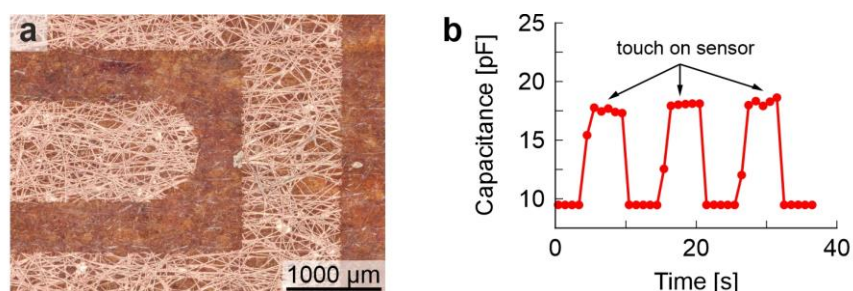


Figure S3. Touch sensor underneath transparent varnish. a) Optical micrograph of the 1 mm wide interdigital electrodes on paper. b) Contact between finger and the transparent surface increases the measured capacitance @1 MHz of the iSen.

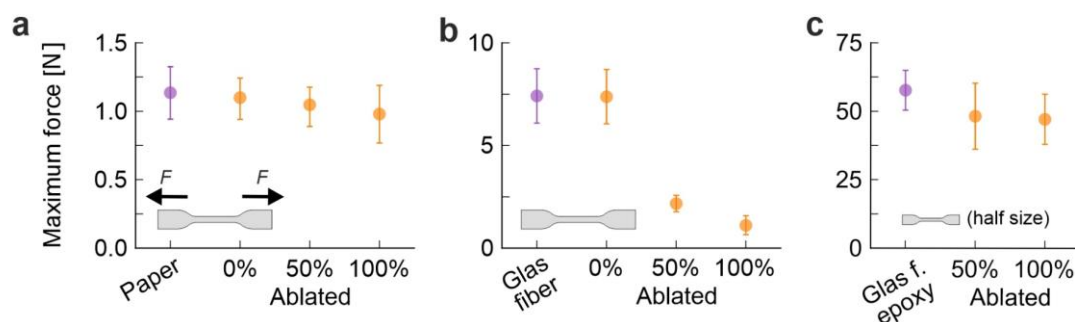


Figure S4. Figure S4. Influence of laser ablation on the mechanical strength of the sensors. The tensile tests were based on the ISO 527-2:2012(E) Type 5A standard. Each specimen was pulled apart to failure using a universal tensile testing machine. The data show the mean and standard deviation of the maximum tensile force of at least six specimens per measurement point. 300 nm copper was deposited as the metal layer. (a) Pure paper and laser-ablated paper sensors with three different degrees of ablation (0, 50 and 100 %). The small inset shows the sample design.

The data show a minimal decrease in mechanical strength with increasing ablated fraction. b) Pure and metallized, non-ablated (0 %) glass fiber shows equally high tensile strength. Semi and fully ablated glass fiber substrates have lower tensile strength due to partial damage on the binder adhesive between the fibers. We note that the structural integrity of the glass fiber sensors is nevertheless given. c) Glass fiber substrate embedded in an epoxy adhesive after the ablation. The sample size was halved because of its high strength. The ablation shows a minimal weakening, which can be also related to the different glass fiber sheets used.

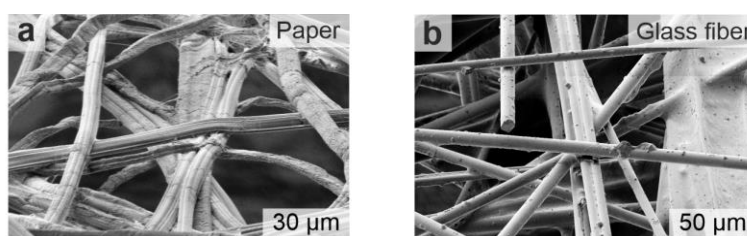


Figure S5. SEM micrographs of the substrate materials used for iSens: a) the paper and glass fiber (b).

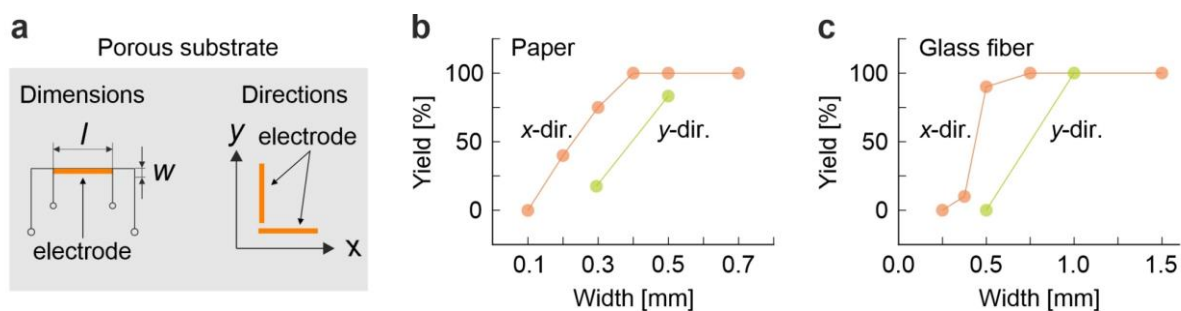


Figure S6. Electrode characterization on the porous substrates. a) The dimensions of the metal electrodes are given by the length l and the width w . The electrodes on the substrate are aligned with either the x - or the y -direction. b) Measurement results of the Cr/Cu electrodes ($l = 30$ mm) with a Cu thickness of 300 nm on paper and on glass fiber (c). Yield 100% indicates that all measured electrodes are working and have a sufficient conductivity. Both substrates possess a preferred direction with better results (denoted as x).

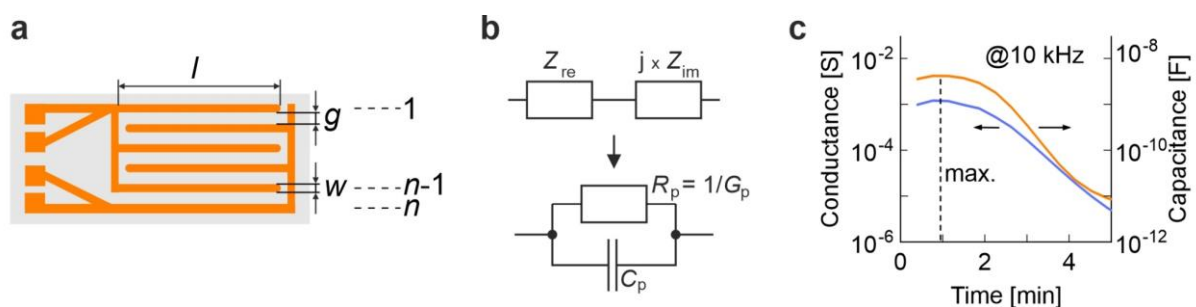


Figure S7. IDE iSen on paper for measuring the curing of a wood glue. a) Dimensions of the impedance sensor. b) The measured impedance data Z_{re} and Z_{im} can be analyzed with a parallel resistor-capacitor model (R_p and C_p , Supporting information section 1.7). c) Conductance G_p and capacitance at the beginning of the measurement. A maximum is reached after about 1 minute.



Figure S8. Preparation and results of the tensile shear test measurements. a) Two wooden plates with a size of $5 \times 125 \times 175 \text{ mm}^3$ were glued together. The sensor was placed in between. b) Four samples were cut out from the glued plates and pulled apart until breakage. c) A sample with a WPF of 100%.

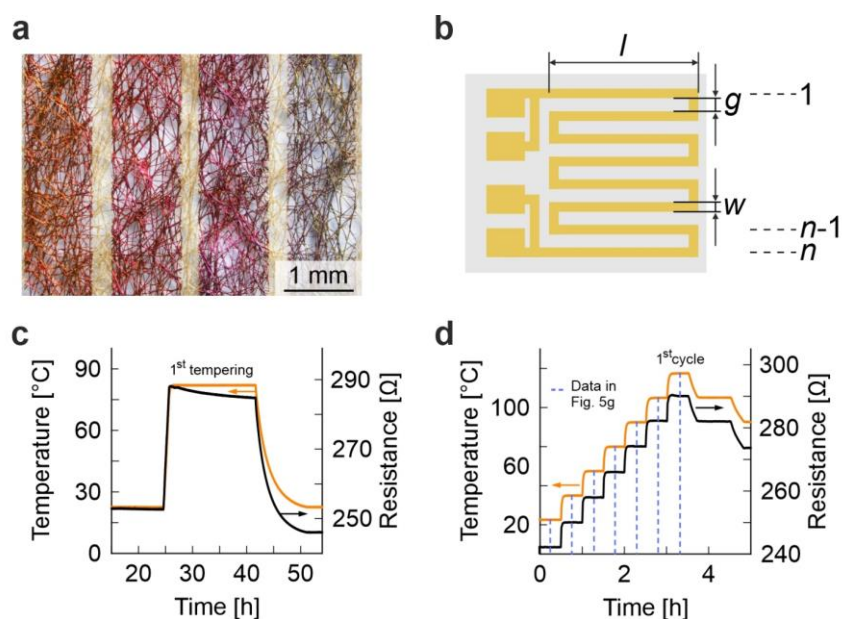


Figure S9. iSens for measuring the temperature during the epoxy curing experiment. a) A copper layer on the paper substrate oxidizes when heated. b) Dimensions of the resistive temperature sensor. c) An annealing effect: sensor resistance decreases during the first tempering. d) Measurement data for the first cycle with step-wise temperature increase. The dashed lines indicate the data points used in Figure 5g.

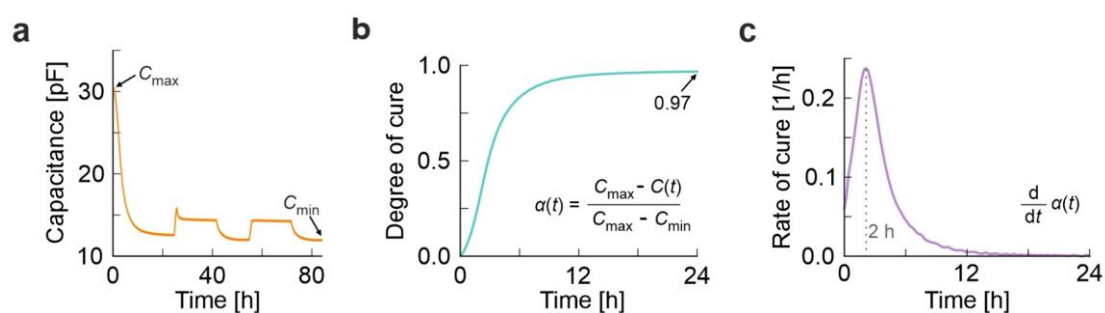


Figure S10. Analysis of the curing kinetics. a) Capacitance @ 1 MHz, measured by the glass fiber sensor SenGZ1 during the epoxy curing-experiment (from the Figure 5e in the main text). The maximal and minimal capacities, C_{\max} and C_{\min} , occur at the beginning and at the end of the measurement. b) Calculated degree of cure α (for the first 24 h), based on references^[33-35]. c) The rate of cure, $d\alpha/dt$, reaches its maximum after two hours.

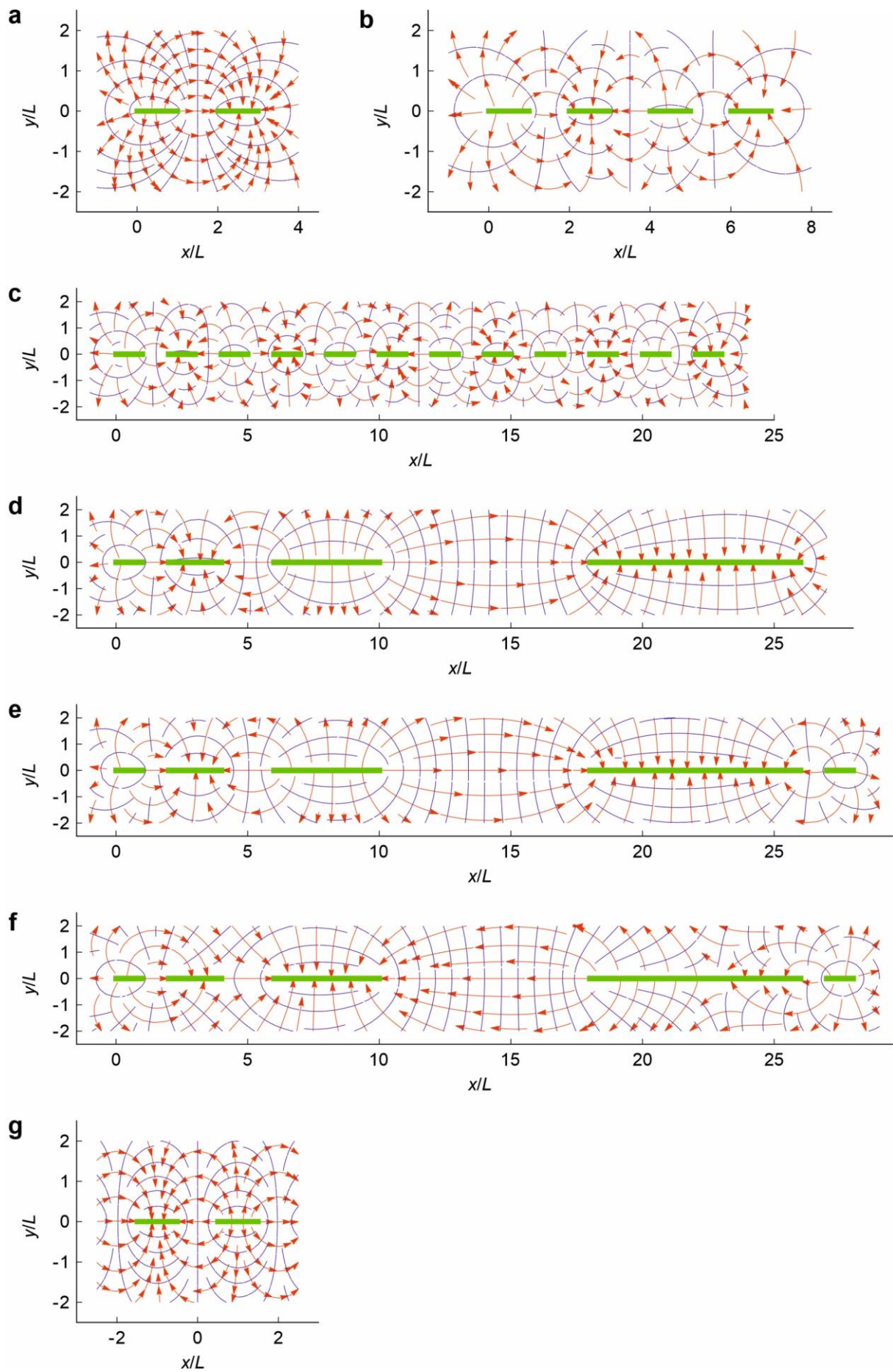


Figure S11. Numerical field (red) and equipotential contour lines (blue) for different sets of strips, based on the algorithm described below the Equation (2). The voltage differences are given in arbitrary units, e.g., [V]. The charges are normalized to the voltage and length values

as $Q^* = \frac{2Q}{\epsilon_0(\epsilon_+ + \epsilon_-)L}$, so that their values for unit voltage difference $U = 1$ (when relevant)

indicate the vacuum capacitance per corresponding strip, see Equation (10); charge value in a “standard” infinite periodic set is 2. a)-c) finite sets of equal strips; d)-f), finite sets of unequal strips, with various prescribed voltage differences, sometimes unequal; g) Infinite periodic system of strips with equal alternating voltages.

a) 2 equal isolated strips. The charges and the capacitance are smaller than for the pair of strips inside an infinite sequence. Voltage difference, starting from the 1st strip, is: (-1). Normalized charges are: (1.563, -1.563).

b) 4 equal strips with prescribed equal alternating voltages. Sequential voltage differences, starting from the 1st strip are: (-1, 1, -1). Normalized charges are: (1.465, -2.062, 2.062, -1.465).

c) Many (12) equal strips with prescribed equal alternating voltages. The edge effects subside after about 3 strips. The appropriate charge value in the infinite periodic structure is 2 (see panel g)). Sequential voltage differences, starting from the 1st strip are: (-1, 1, ..., 1, -1). Normalized charges are: (1.424, -2.111, 1.954, -2.023, 1.989, -2.003, 2.003, -1.989, 2.023, -1.954, 2.111, -1.424).

d) 4 unequal strips with prescribed equal alternating voltages. The charge values are surprisingly stable with respect to the variation in stripe sizes. This reflects the fact, that in the periodic arrangement, the capacitance per pair of strips does not depend on the strip width and gap between them. Sequential voltage differences, starting from the 1st strip are: (-1, 1, -1). Normalized charges are: (1.558, -2.370, 2.086, -1.274).

e) Odd number (5) of *unequal* strips with prescribed *equal* alternating voltages, the charges are significantly redistributed. Sequential voltage differences, starting from the 1st strip are: (-1, 1, -1, 1). Normalized charges are: (1.490, -2.436, 1.950, -2.731, 1.726).

f) Same geometry as above, but with *unequally* varying voltages, prescribed by hand. The algorithm works correctly for these values. In the very general case further adjustment of the square root branches may be required. Sequential voltage differences, starting from the 1st strip are: (-2, -1, 4, 3). Normalized charges are: (3.089, -2.635, -6.692, -0.561, 6.799).

g) 2 adjacent strips in an infinite periodic set. The voltage difference is (1). Normalized charges are (-2, 2). Compare with the similar equidistant finite sets in Figure a-c.

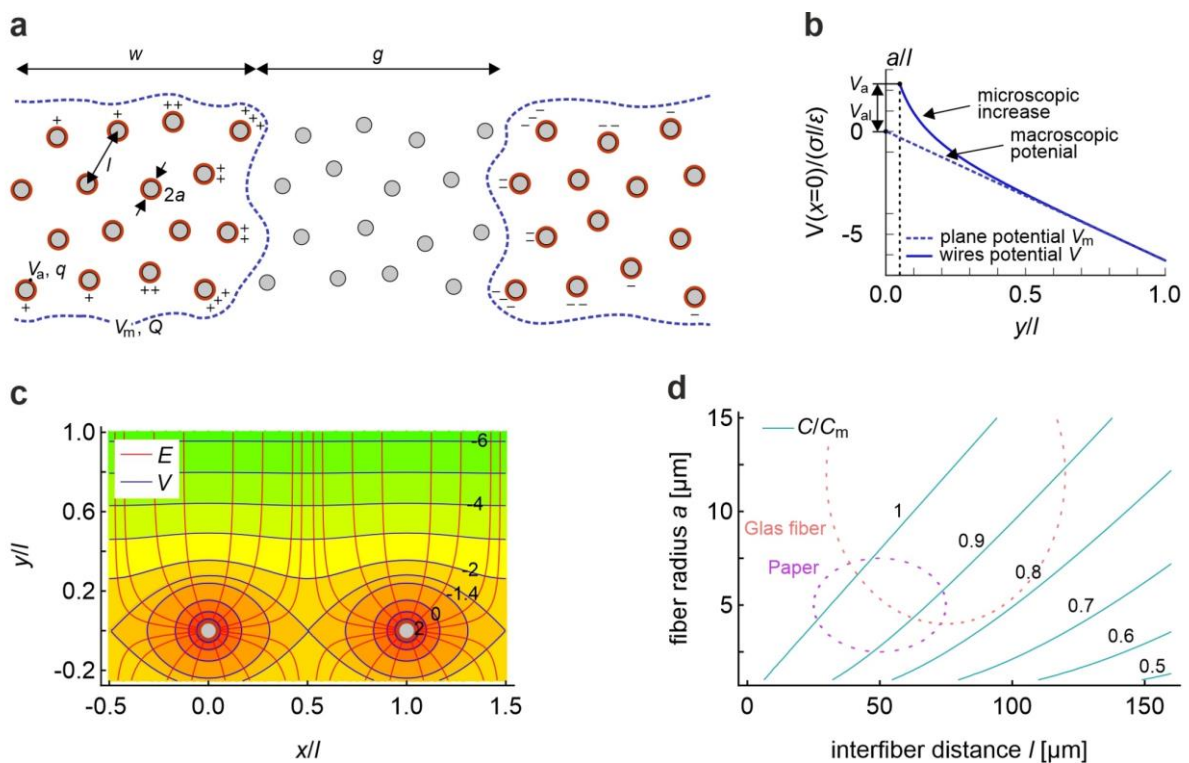


Figure S12. The influence of the sensor structure: a) macroscopic potential around the metallized fibers; b) macroscopic and true potential in the minimal model (c), and d) the resulting capacitance correction.

a) Schematic cross-section of the sensor fine structure. Metallized fibers have an (average) outer radius a , and inter-fiber distance $l \gg a$. L is the length of the structure perpendicular to the

plane of the figure. All fibers have the same voltage, but are unevenly charged. Those in the bulk carry virtually no charge, as they are effectively screened within the “bulk conductor”. Those along the perimeter have higher charge near the edges (needle effect with an $1/\sqrt{x}$ charge singularity near the planar ends of each strip, see also Equation (1)₁). At a distance about l from the outermost fibers, the potential smoothens to its macroscopic value V_m , which enters the macroscopic capacitance formulas. The true potential on the fibers, V_a , is higher, due to logarithmic increase in cylindrical potential, as one moves from l to a near each individual fiber.

b) Minimal model problem. The electrodes consist of a periodic chain of identical metallized fibers, shown in c). The macroscopic potential (dashed line) is that of an equivalent homogeneously charged plane, and is chosen to have $V_m = 0$ in the plane of fibers at $y = 0$. The true potential V (solid curve) increases logarithmically towards the fiber surface $y = a$ (along $x = 0$) and has the value V_a there. The difference $V_{al} = V_a - V_l$ should be accounted for in the capacitance formulas. It can be calculated from the charge on each fiber q , which is defined by the density of fibers and the overall charge on the electrode Q . The latter is related to the macroscopic voltage V_m via macroscopic capacitance C_m .

c) Color-coded normalized potential (V , blue) and electric field lines (E , red) near the periodic set of equally charged fibers, infinitely long in the direction perpendicular to the Figure plane. The full red curve in Figure S12b corresponds to the potential along the vertical line $y > a$, in this plot, starting from the fiber, positioned at $x = 0$.

d) The ratio of the true and the macroscopic capacitances C/C_m calculated using Equation (20)₂ for $w = g = 300\mu\text{m}$, as a function of the (average) inter-fiber distance l and radius a . For thin fibers and/or large l the correction is significant. The dashed ovals indicate the approximate ranges of (average, effective) fiber radii and inter-fiber distances for the paper- and glass fiber-based sensors. Bundled fibers (which are common for both cases, see Figure 2b-e and Figure

S5) should be treated as a single fiber with larger effective radius. The model is applicable to the right of the contour line “ l ”, where $l \gg a$. For our numbers, the expected decrease in capacitance is below 10-20% at most.

4. Tables

Table S1. iSen materials, parameters and designs.

| Name | Substrate | Electrode material | Design or Function: impedance Z or resistance R | Electrode or line number n | Electrode or line length l [mm] | Electrode width w [mm] | Electrode gap g [mm] | Shown in Figure | Information |
|---------|-------------|--------------------|---|------------------------------|-----------------------------------|--------------------------------|------------------------|-------------------------------|---|
| Sen-GR1 | glass fiber | Cr/Ag | R | 12 | 16 | 1 | 0.5 | 1b,i & 5a | temp. sensor and heater in epoxy experiment |
| Sen-GR2 | glass fiber | Cr/Cu | R | 1 | 5, 10, 15, 20, 25, 30 | 0.25, 0.375, 0.5, 0.75, 1, 1.5 | - | 2i,j | electrode characterization |
| Sen-GZ1 | glass fiber | Cr/Ag | Z | 11 | 25 | 1 | 0.5 | 2d,e & 5a | impedance sensor in epoxy experiment |
| Sen-GZ2 | glass fiber | Cr/Cu | Z | 15 | 5, 10, 15, 25 | 1 | 0.5 | 2h | sensor characterization |
| Sen-GZ3 | glass fiber | Cr/Cu | Z | 1, 2, 3, 4, 6, 8, 10, 12, 15 | 25 | 1 | 0.5 | 2k | sensor characterization |
| Sen-NZ1 | no | ideal metal | Z | 2 | 4.86 | 0.3 | 0.3 | 3b,c | FEM simulation |
| Sen-PR1 | paper | Cr/Cu | R | 14 | 16 | 1 | 0.2 | S9a | oxidized |
| Sen-PR2 | paper | Cr/Cu | R | 1 | 5, 10, 15, 20, 25, 30 | 0.1, 0.2, 0.3, 0.4, 0.5, 0.7 | - | 2f,g | electrode characterization |
| Sen-PZ1 | paper | Cr/Cu | Z | 25 | 25 | 0.3 | 0.3 | 1a,h & 2b,c & 4a & ToC figure | impedance sensor in wood experiment |
| Sen-PZ2 | paper | Cr/Cu | Z | 11 | 25 | 1 | 0.5 | 1j & S3a | touch sensor |
| Sen-PZ3 | paper | Cr/Cu | Z | 15 | 5, 10, 15, 25 | 1 | 0.5 | 2h | sensor characterization |
| Sen-PZ4 | paper | Cr/Cu | Z | 1, 2, 3, 4, 6, 8, 10, 12, 15 | 25 | 1 | 0.5 | 2k | sensor characterization |

Table S2. Measurement results of the tensile shear tests.

| Material | Shear strength [MPa] | Wood failure percentage (WFP) [%] | Ultimate strain at shear strength [%] |
|-------------------------|----------------------|-----------------------------------|---------------------------------------|
| Polyimide (no adhesion) | 0 ± 0 | 0 ± 0 | 0 ± 0 |
| Paper | 3.76 ± 4.89 | 8.33 ± 28.87 | 0.32 ± 0.18 |
| HP Paper | 13.43 ± 1.36 | 81.25 ± 37.3 | 0.61 ± 0.06 |
| Control | 13.54 ± 0.71 | 100 ± 0 | 0.58 ± 0.05 |

References

- [1] R. Igreja, C. J. Dias, *Sensor Actuat a-Phys* **2004**, 112, 291.
- [2] E. Danicki, Y. Tasinkevych, *Sensors-Basel* **2012**, 12, 11946.
- [3] E. Danicki, *Spectral theory of interdigital transducers*, <http://bluebox.ippt.pan.pl/~edanicki/danickibook.pdf> **2007**.
- [4] E. J. Danicki, Y. Tasinkevych, *Mikon Conference Proceedings* **2008**, 1-2, 481.
- [5] E. L. Danicki, Y. Tasinkevych, *J Electrostat* **2006**, 64, 386.
- [6] A. P. Prudnikov, I. U. A. Brychkov, O. I. Marichev, *Integraly i riady: Elementarnye funktsii*, "Nauka," Glav. red. fiziko-matematicheskoi lit-ry, Moskva **1981**.
- [7] F. Molina-Lopez, T. Kinkeldei, D. Briand, G. Troster, N. F. de Rooij, *J. Appl. Phys.* **2013**, 114.
- [8] R. Igreja, C. J. Dias, *Sensor Actuat B-Chem* **2006**, 115, 69.
- [9] R. K. Hoffmann, H. H. Howe, *Handbook of microwave integrated circuits*, Artech House, Norwood, MA **1987**.
- [10] H. A. Wheeler, *Ieee T Microw Theory* **1964**, Mt12, 280.
- [11] H. A. Wheeler, *Ieee T Microw Theory* **1965**, Mt13, 172.
- [12] H. A. Wheeler, *Ieee T Microw Theory* **1977**, 25, 631.
- [13] Y. Yang, G. Chiesura, T. Vervust, J. Degrieck, J. Vanfleteren, *J Polym Sci Pol Phys* **2016**, 54, 2028.
- [14] S. B. Cohn, *IRE Transactions on Microwave Theory and Techniques* **1960**, 8, 638.
- [15] N. Davy, *Philos Mag* **1944**, 35, 819.
- [16] Y. Feng, J. Hallstedt, Q. A. Chen, L. R. Zheng, Y. P. Huang, *IEEE Sensors* **2009**, 1-3, 1034.
- [17] S. S. Gevorgian, T. Martinsson, P. L. J. Linner, E. L. Kollberg, *Ieee T Microw Theory* **1996**, 44, 896.
- [18] D. V. Sivukhin, *Obshchii kurs fiziki*, Fizmatlit, **2005**.
- [19] P. M. Morse, H. Feshbach, *Methods of theoretical physics*, McGraw-Hill, Boston, Mass. **1999**.
- [20] V. P. Veiko, V. I. Konov, in *Springer Series in Materials Science*, Springer International Publishing : Imprint: Springer, Cham **2014**, 1 online resource (XVII).
- [21] S. M. Metev, V. P. Veiko, *Laser-assisted microtechnology*, Springer, Berlin ; New York **1998**.
- [22] D. Bäuerle, *Laser processing and chemistry*, Springer, Heidelberg ; New York ; **2011**.
- [23] W. M. Steen, J. Mazumder, *Laser Material Processing*, Springer, London **2010**.
- [24] A. Blom, P. Dunias, v. P. Engen, W. Hoving, *Proc. SPIE* **2003**, 4977, 493.

- [25] M. Colopi, A. G. Demir, L. Caprio, B. Previtali, *International Journal of Advanced Manufacturing Technology* **2019**, 104, 2473.
- [26] A. Hess, R. Schuster, A. Heider, R. Weber, T. Graf, *Lasers in Manufacturing 2011: Proceedings of the Sixth International Wlt Conference on Lasers in Manufacturing, Vol 12, Pt A* **2011**, 12, 88.
- [27] N. Arnold, N. Bityurin, *Appl Phys a-Mater* **1999**, 68, 615.
- [28] Z. Toth, B. Hopp, T. Szorenyi, Z. Bor, E. A. Shakhno, V. P. Veiko, *Computer-Controlled Microshaping* **1999**, 3822, 18.
- [29] A. L. Buck, *Journal of Applied Meteorology* **1981**, 20, 1527.
- [30] V. Oja, E. M. Suuberg, *Analytical Chemistry* **1997**, 69, 4619.
- [31] R. Radvan, M. Castillejo, P. Pouli, J. F. Asmus, A. Nevin, "Lasers in the Conservation of Artworks VIII", presented at *LACONA VIII*, Romania, **2009**.
- [32] J. Nimmrichter, W. Kautek, M. Schreiner, *Lasers in the conservation of artworks : LACONA VI proceedings : Vienna, Austria, Sept. 21-25, 2005*, Springer, Berlin ; New York **2007**.
- [33] M. Sernek, F. A. Kamke, *International Journal of Adhesion and Adhesives* **2007**, 27, 562.
- [34] G. Levita, A. Livi, P. A. Rolla, C. Culicchi, *Journal of Polymer Science Part B: Polymer Physics* **1996**, 34, 2731.
- [35] R. Casalini, S. Corezzi, A. Livi, G. Levita, P. Rolla, *Journal of Applied Polymer Science - J APPL POLYM SCI* **1997**, 65, 17.